Effective integration of reservoir rock-typing and simulation using near-wellbore upscaling

Accepted Manuscript

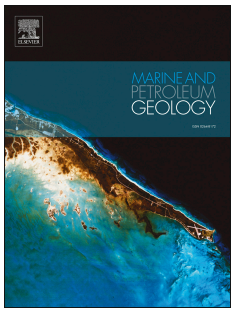

Effective integration of reservoir rock-typing and simulation using near-wellbore upscaling

Viswasanthi Chandra, Andrew Barnett, Patrick Corbett, Sebastian Geiger, Paul Wright, Richard Steele, Paul Milroy

PII: S0264-8172(15)00154-3

DOI: 10.1016/j.marpetgeo.2015.05.005

Reference: JMPG 2233

To appear in: *Marine and Petroleum Geology*

Received Date: 1 August 2014

Revised Date: 4 May 2015

Accepted Date: 7 May 2015

Please cite this article as: Chandra, V., Barnett, A., Corbett, P., Geiger, S., Wright, P., Steele, R., Milroy, P., Effective integration of reservoir rock-typing and simulation using near-wellbore upscaling, Marine and Petroleum Geology (2015), doi: 10.1016/j.marpetgeo.2015.05.005.

Effective integration of reservoir rock-typing and simulation using near-wellbore upscaling

*Viswasanthi Chandra[1, 2], Andrew Barnett[3], Patrick Corbett[1, 2], Sebastian Geiger[1, 2], Paul Wright[3], Richard Steele[3], Paul Milroy[3]

1. Institute of Petroleum Engineering, Heriot-Watt University, Riccarton, Edinburgh, EH14 4AS, UK.

2. International Centre for Carbonate Reservoirs

3. BG Group, 100 Thames Valley Park, Reading, RG6 1PT, UK.

*Corresponding author (e-mail: viswa.chandra@pet.hw.ac.uk)

Keywords: carbonate reservoirs, rock-typing, near-wellbore upscaling, initialisation, permeability, relative permeability, capillary pressure, J function

Abstract

Obtaining a fit-for-purpose rock-type classification that adequately incorporates the key depositional and diagenetic heterogeneities is a prime challenge for carbonate reservoirs. Another prevailing issue is to integrate the static and dynamic data consistently with the rock-typing scheme in order to correctly initialise the reservoir flow simulation model. This paper describes a novel near-wellbore rock-typing and upscaling approach adopted to address the crucial challenges of integrating reservoir rock-typing and simulation in carbonate reservoirs. We demonstrate this workflow through a case study for a highly heterogeneous Eocene-Oligocene limestone reservoir, Field X. Geological studies carried out in Field X suggested that the key permeability pathways are strongly related to the mechanism of reservoir porosity and permeability evolution during late-burial corrosion. The rock-typing and upscaling methodology described in this paper involves the geological-petrophysical classification of the key reservoir heterogeneities through systematic evaluation of the main paragenetic events. Associations between the depositional and late-burial corrosion features, and their impact on reservoir flow properties, were accounted for in our workflow. Employing near-wellbore rock-typing and upscaling workflow yielded consistent initialisation of the Field X reservoir simulation model and therefore improved the accuracy of fluids-in-place calculation. Subsequently, the cumulative production curves computed by the reservoir simulation model of Field X showed closer agreement to the historic production data. The revised Field X simulation model is now much better constrained to the reservoir geology and provides an improved geological-prior for history matching.

1. Introduction

Rock-typing describes the process of characterising geological facies in terms of their dynamic behaviour. It is highly challenging to obtain a fit-for-purpose rock-typing scheme that adequately represents the influence of diagenetic processes on the reservoir petrophysical properties, fluid in-place volumes, and hydrocarbon recovery efficiency. This is a classic issue for carbonate reservoirs, which typically contain multi-scale and multi-modal pore types that are difficult to be adequately incorporated into rock-typing (e.g. Gomes et al. 2008; Hollis et al. 2010; van der Land et al. 2013; Skalinski & Kenter 2015). Another common challenge is to integrate the dynamic data during rock-typing and upscale the petrophysical properties of the rock types to the reservoir model scale using appropriate geostatistical tools to correctly initiate the reservoir simulation model. Furthermore, the difficulties of predicting reservoir quality variations at inter-well scales have long hindered the efficacy of carbonate reservoir rock-typing and simulation (c.f. Agar & Geiger 2015).

Numerous authors have proposed carbonate rock-typing workflows, trying to address the challenges discussed above. Gomes et al (2008) discussed the importance of obtaining good understanding of the depositional and diagenetic processes in order to establish better links between lithofacies, petrophysical groups and rock types. Hollis et al (2010) demonstrated a rock-typing workflow based on pore system characterisation such that each rock type could be defined on the basis of both its petrophysical properties and behaviour during hydrocarbon recovery. Van der Land et al (2013) proposed a general approach towards carbonate rock typing through pore-scale forward modelling of the paragenetic sequences. Skalinski & Kenter (2015) proposed a carbonate petrophysical rock-typing workflow that could account for the role of diagenetic processes on reservoir dynamics, and could also account for the role of fractures. In contrast, the work presented in this paper is aimed to address all of the above issues through an integrated near-wellbore rock-typing and upscaling approach. The novel aspect of the Near-Wellbore Upscaling (NWU) methodology applied in our study is that it enabled explicit modelling of typical multi-scale carbonate heterogeneities such as leaching, stylolites and associated small-scale fractures, which are difficult to account for in existing reservoir rock-typing and simulation workflows. Our methodology allows us to model these multi-scale geological-petrophysical features more robustly at the reservoir grid-block scale in a reservoir simulation model. The rock-typing and upscaling methodology described in this study involves the geological-petrophysical classification of multi-scale heterogeneities in the studied reservoir through systematic evaluation of the key paragenetic events with consideration to the crucial parameters of near-wellbore modelling and upscaling workflow.

1.1. Case study: Rock-typing and simulation challenges in Field X

Field X is a giant offshore oil and gas field comprising an Eocene-Oligocene limestone reservoir with long production history. It has a broad, low relief anticline trap structure and consists of a gas column

up to 50 m thick, an oil rim of about 20 m thickness, and an underlying aquifer. Permeability has been identified as one of the biggest uncertainties associated to Field X's reservoir simulation model during previous field studies (Chandra 2014; Chandra et al. 2015). In addition, the performance predictions were also found to be sensitive to the volumes of fluids initially-in-place and the critical oil saturation. Major modifications of the reservoir model were required in order to obtain a history match. These modifications were not necessarily based in the reservoir geology but comprised numerical adjustments in the dynamic model. For example, horizontal permeability multipliers of 10 and 20 had to be applied in the main reservoir zones, along with multipliers at the wells (Oates et al. 2012; Chandra 2014; Chandra et al. 2015). Chandra et al. 2015 demonstrated how the computed cumulative oil production decreased when the permeability modifications were removed in the dynamic model (Figure 1). The irregularities observed between the distributions of fluids based on reservoir simulation predictions and the actual production volumes also imply that the in-place volumes and production characteristics were not properly understood (Calvert & Ballay 2011). It was hence deemed necessary to re-evaluate the geological-petrophysical model of Field X to increase the reliability of oil-in-place calculations and reservoir model initialisation for simulation predictions.

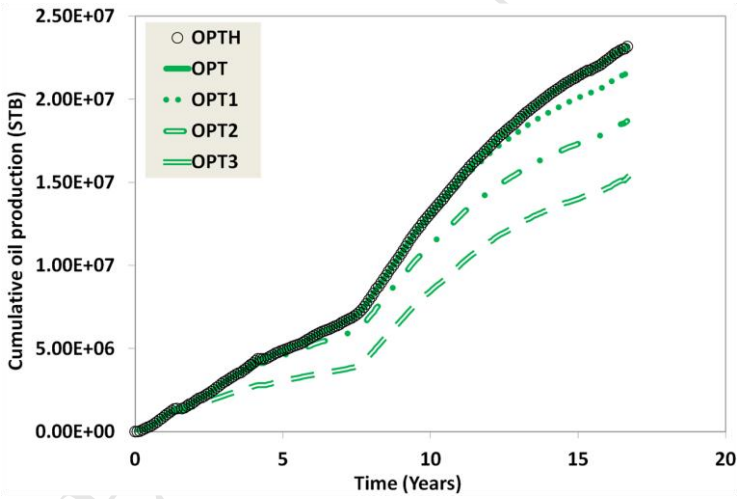

Fig. 1. Cumulative oil production curves from Field X. OPT corresponds to the history matched simulation model, which yields a cumulative oil production that is identical to the historic production data OPTH. OPT1 is the simulated production after removing horizontal permeability multipliers (K-multipliers) from the zones. OPT2 is the simulated production after removing zone and local well K-multipliers. OPT3 is the simulated production after removing the well productivity multipliers in addition to the zone and well K-multipliers. STB is the abbreviation for 'Stock Tank Barrels'. Figure modified from Chandra et al. 2015.

Geological studies carried out by the operator suggest that the key static and dynamic reservoir properties in Field X are strongly related to the mechanism of reservoir porosity-permeability evolution during late-burial corrosion (Wright & Barnett 2011). In this study, late-burial corrosion is referred to as deep burial/mesogenetic corrosion associated with the corrosion of limestone by burial-derived (hypogene) fluids. The uncertainty associated with permeability modelling in Field X was discussed by Oates et al. (2012), Chandra (2014) and Chandra et al (2013b & c, 2015). Chandra et al.

(2015) demonstrated that re-evaluating the permeability model of Field X with considerations to late diagenetic corrosion can significantly improve the reservoir simulation model. The key porosity types present in Field X, such as chalky microporosity, macroporosity including vuggy and moldic pores, leached stylolites and associated tension gashes, were caused by late burial (mesogenetic) dissolution (Wright & Barnett 2011). Note that microporosity in Field X is defined as pores with a pore throat diameter of 0.5 microns or less.

In order to revise the geomodel of Field X with considerations to the proposed late-burial corrosion model (Wright & Barnett 2011), it is vital to obtain a fit-for-purpose rock-typing scheme that adequately incorporates the late-burial corrosion heterogeneities. However, conventional rock-typing workflows may not be appropriate to Field X due to the difficulties associated with the petrophysical characterisation and data sampling of the key porosity types such as leached stylolites and associated tension gashes. Besides, upscaling these sub-grid-scale heterogeneities to incorporate them adequately into the reservoir simulation model is another major challenge. The available core plug data suffers from inherent sample bias and insufficiency due to rock-mechanical constrictions and due to the shortcomings of using a regular sampling interval of 1 meter (Oates et al. 2012). Due to these challenges, Field X provides an ideal case study for the application of the near-wellbore rock-typing and upscaling methodology. In this study, we thus aim to employ the near-wellbore rock-typing and upscaling methodology to revise the full field geomodel of Field X and generate a properly initialised reservoir simulation model with consistent static and dynamic reservoir properties.

1.2. Field X depositional and diagenetic history

Field X has a broad, low-relief anticlinal trap structure and comprises an Eocene-Oligocene limestone reservoir (Figure 2a) with an oil rim and an underlying aquifer. The offshore basin comprising Field X is a passive margin basin, split into longitudinal horst and graben stripes by a series of basement controlled NorthWest-SouthEast to North-South trending faults. The major structural feature in the block containing Field X and its neighbouring hydrocarbon fields is the East-fault zone (Figure 2b). Figure 2b shows the porosity model of Field X and the four wells used in this study. Porosity and permeability came from Routine Core Analysis (RCA) while capillary pressure and relative permeability data used in this work were part of the measured Special Core Analysis (SCAL) data. RCA and SCAL were both provided by the operator. The original geomodel of Field X and the history matched simulation model were provided by the operator. The original model of Field X did not involve any rock-typing scheme. The geomodel comprises over five million grid blocks and a total of 59 layers. The grid block dimensions are 50 m x 50 m horizontally and an average of 2 m vertically. The two main zones in Field X hosting oil and gas are the Early Oligocene A Zone and the Eocene B Zone. The oil-water contact and the gas-oil contact are present in the B Zone. The stratigraphic framework of these zones was interpreted to be a stacked depositional sequence in a

shallow ramp setting (Figure 2c). A Zone and B Zone are separated by a disconformity that is associated with sub-aerial exposure corresponding to an early Oligocene fall in relative sea level. A shale unit, which we refer to as 'A/B supra-unconformity shale', overlies this disconformity and acts as transient local seal, capping the B Zone. Outer ramp Nummulitic facies are the dominant facies in the A Zone. In contrast, the B Zone mainly consists of inner ramp Coskinolina assemblage. A Zone and B Zone were interpreted to be of different depositional systems and were hence treated separately throughout the rock-typing workflow employed in this study.

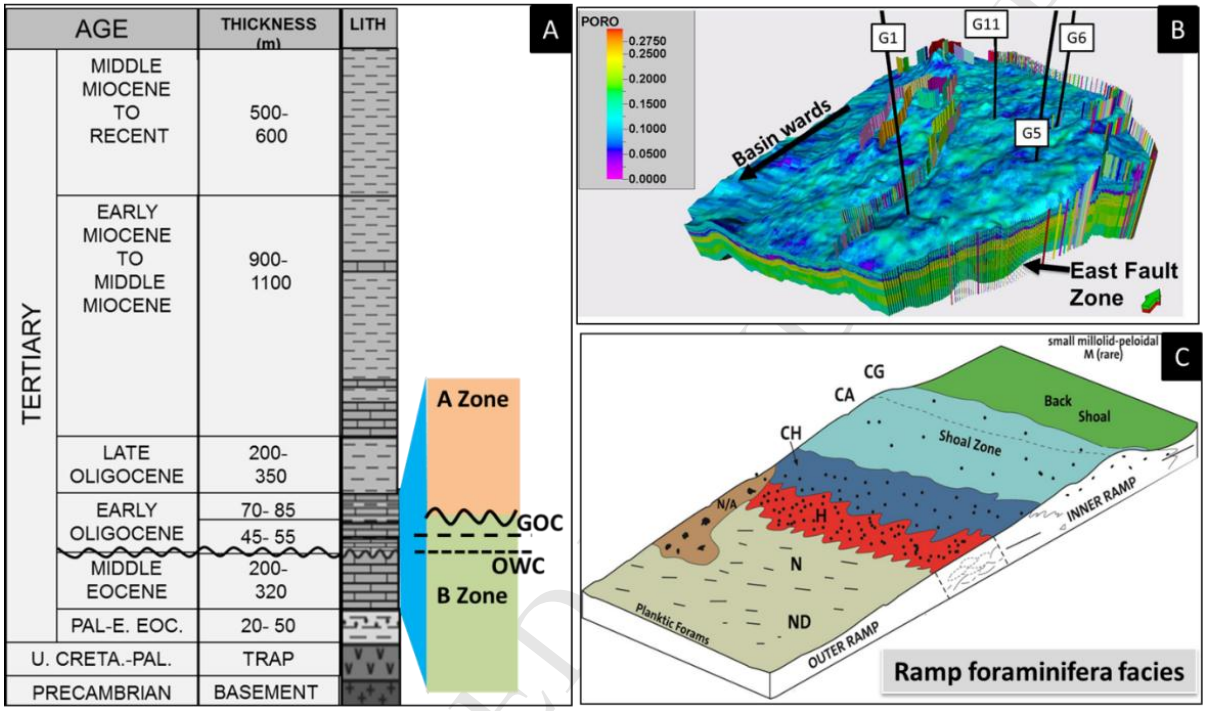

Fig. 2. (a) Stratigraphic summary of Field X showing the main reservoir units A Zone and B Zone, the gas-oil contact (GOC) and the oil water contact (OWC) (Chandra 2014). **(b)** Field X geomodel showing the porosity distribution, main fault zones present in the model and the four wells used in this study. The East fault zone is the major structural feature in the block containing Field X and its neighbouring hydrocarbon fields (Chandra 2014). **(c)** Illustration of foraminifera distribution in the limestones of Field X with reference to a carbonate ramp model zone. Facies key; CG- *Coskinolina* grainstones; CA- *Coskinolina* and *Alveolinid* facies; CH- *Coskinolina* hash facies; M- *Miliolid* facies; H- Hash facies with fine skeletal debris; N- *Nummulites* matrix-rich limestones, ND- *Nummulites-Discocyclinid* facies. Modified from Wright & Barnett (2011).

The main paragenetic events that occurred in Field X were discussed by Wright & Barnett (2011) and are summarised in (Figure 3). The A Zone underwent deeper phreatic stabilisation after deposition, whereas the B Zone sediments were stabilised and cemented under shallow burial conditions. During intermediate burial, pressure dissolution features such as stylolites, microstylolites and clay seams developed ubiquitously. The majority of the stylolites were associated with tension gashes, some of which were cemented (Moshier 1989; Alsharhan 1990; Alsharhan & Sadd 2000). It was hypothesised that the stylolites later reopened during a tectonic uplift event, allowing them to act as conduits for burial-derived fluids that caused a major phase of late-burial (mesogenetic) dissolution. During this

process the stylolites and associated tension gashes could have conducted reactive fluids containing sulphides, silica and aluminium, enabling them to migrate into the surrounding host limestones. These reactive fluids corroded the formerly tight cemented matrices by selectively removing the micritic grains with high surface area (Wright & Barnett 2011). The conduits feeding the reactive fluids to the reservoir are not known with certainty. Feed through faults and from the closely underlying basement are both possible. The presence of exotic minerals in the core such as pyrite, dickite and saddle dolomite supports mixing corrosion mechanism as defined by Esteban & Taberner (2003). Late-burial dissolution (Esteban & Taberner 2002 and 2003) played a crucial role in the evolution of reservoir static and dynamic properties in Field X (Wright & Barnett 2011).

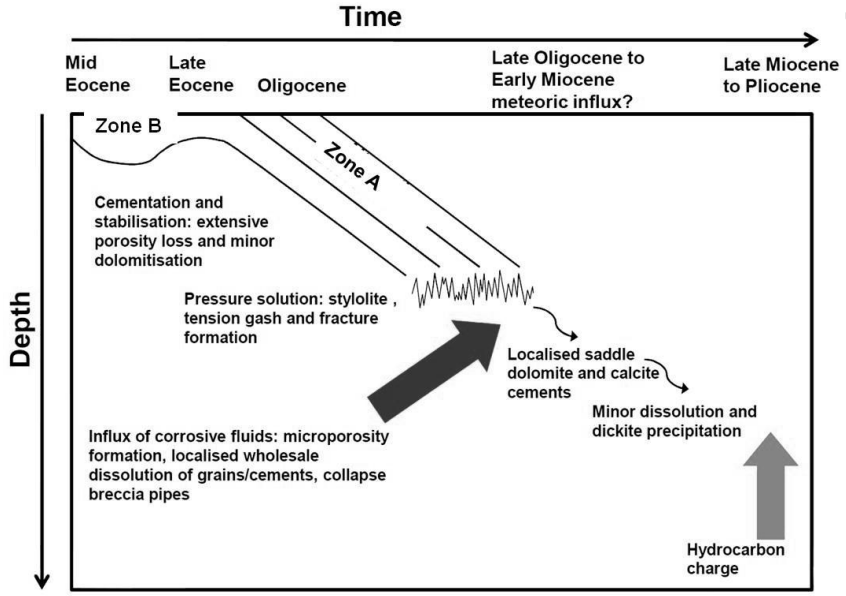

Fig. 3. Key paragenetic events that occurred in A Zone and B Zone (modified from Wright & Barnett 2011). The depositional facies underwent extensive early cementation followed by compaction and pressure solution developing stylolites and associated tension gashes. This was followed by a major phase of dissolution associated with saddle dolomite and dickite precipitation.

The main porosity types present in Field X and probably the majority of the reservoir porosity originated as a result of late-burial corrosion of the A Zone and B Zone limestones. The key porosity types associated with late-burial corrosion are well connected micro- and macro-pore networks with leached stylolite and tension gash porosity, all of which have significant impact on fluid flow in the reservoir (Figure 4) (Wright & Barnett 2011; Chandra et al. 2015). The tension gashes observed in the core were at times upto 6 mm wide and usually aligned with the direction of the stylolite peaks. They seemed to have initiated from the mechanical discontinuity along the stylolite surface and developed along the direction of the lithostatic stress. Earlier geological studies suggest the presence of two generations of tension gashes, the most recent ones tending to be open or partially filled with dickite and calcite. Hence the two types of 'fracture porosity' observed in Field X are; a) Stylolite associated tension gashes, which are few mm to several cms long and visible only on or below core-scale resolution and b) 30-40 cm long fractures with no direct relation to stylolites that truncate the

stylolites and tension gashes and can be seen in FMI logs. This type of fractures was rarely observed in the studied wells. In this paper, the porosity types associated with late-burial dissolution are hereafter referred to as corrosion-enhanced porosity (CEP). Figure 5 illustrates the conceptual model of the multiscale connectivity of the CEP zones visualised across the Field X reservoir. In effect, the rock-typing methodology we have adopted for Field X was based on the hypothesis that the enhanced permeability in Field X was caused by late-burial corrosion, which needed to be accounted for in the geomodel and reservoir simulation model.

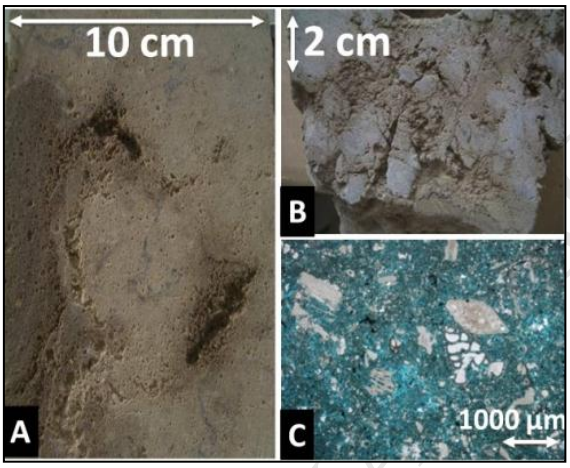

Fig. 4. Illustration of varying scales of corrosion-enhanced porosity caused by late burial corrosion within the corrosion-enhanced porosity (CEP) zones in A and B Zones (modified from Chandra et al. 2015). **(a)** Vuggy/moldic porosity on core. **(b)** Leached stylolite and associated tension gashes. **(c)** Matrix micro- and macroporosity observed in thin-section.

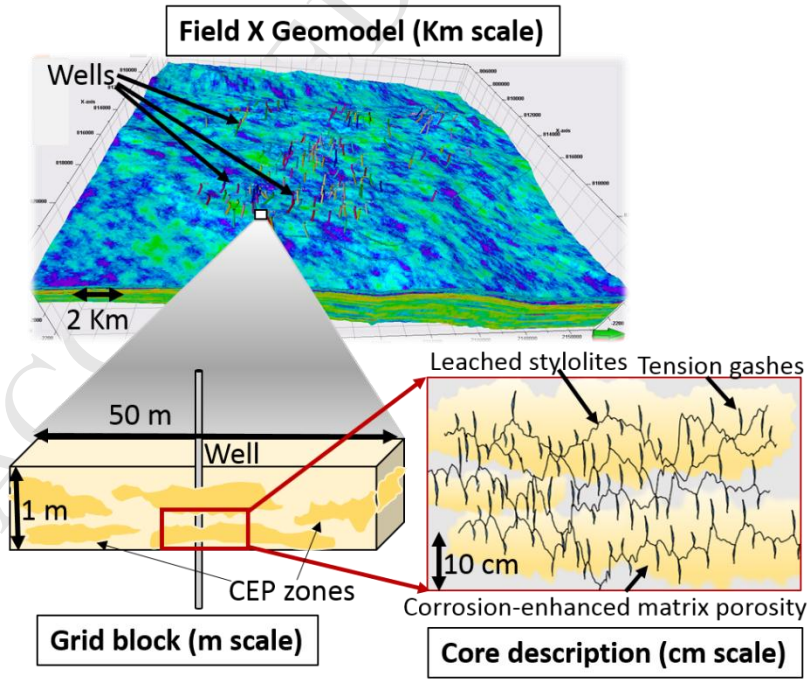

Fig. 5. Illustration of the conceptual model of multiscale connectivity of the CEP zones across the Field X reservoir. The leached stylolites or tension gashes alone may not act as the high permeability conduits, but rather the combination of the corrosion-enhanced matrix porosity, stylolites and tension gashes is the potential contributor to the enhanced permeability in Field X.

2. Near-wellbore rock-typing and upscaling workflow

In order to facilitate the effective description of this workflow, we have defined some key terminology at the outset. Lithofacies is defined as depositional facies classified based on sedimentary texture, grain types and depositional structure (Dunham 1962). A 'geological rock type', GeoRT, is a division of a lithofacies type that went through similar diagenetic processes and whose pore network has the same genetic origin. A 'near-wellbore rock type', NWRT, is a bin of GeoRTs that have similar petrophysical properties at core scale and near-wellbore modelling (NWM) aspects. A 'Geological-Porosity Derived System', GeoPODS, is a geologically realistic equivalent of the 'hydraulic flow unit' (c.f. Amaefule et al. 1993) at the reservoir grid-block scale. It consists of a bin of NWRTs that went through a near-wellbore upscaling workflow and display similar static and dynamic properties.

The rock-typing approach we adopted was iterative to ensure seamless integration of the multi-scale and multi-disciplinary datasets. First, we classified the geological rock types (GeoRTs) by characterising and grouping the gross depositional facies and the key porosity types associated with late-burial dissolution. This was guided by the depositional model and interpretation of paragenetic sequences that occurred in the reservoir. The GeoRTs in our study are hence comparable to the rock types developed by Hollis et al (2010) who grouped the lithofacies of the same genetic origin and pore network to ensure that the entire geological evolution of the rock (including the diagenetic history) is incorporated into the rock type definition. The GeoRTs were then grouped into 'near-wellbore rock types' (NWRTs) based on their petrophysical characterisation using the RCA and SCAL data. This was done with consideration to the NWM aspects of the GeoRTs to facilitate their input into the near-wellbore upscaling workflow. Near-wellbore upscaling yields averaged petrophysical properties at the reservoir simulation grid-block scale.

Following near-wellbore upscaling, the centimetre-scale NWRTs were further binned into reservoir-scale 'Geological-Porosity Derived Systems' (GeoPODS) based on their upscaled petrophysical properties. In this work, GeoPODS emphasise the geological basis for the grouping and upscaling of rock types and are coherent with the definition of Porosity Derived Systems (PODS) (Kazemi et al. 2012) at the reservoir grid block scale. Thus, GeoPODS represent the impact of sub-grid scale heterogeneities on fluid flow at the reservoir grid-block scale and help define the Global Hydraulic Elements (c.f. Corbett & Potter 2004) concept at the appropriate modelling scale for full field simulation models. The evolution of GeoPODS is strongly linked to GeoRTs, which in turn are based on the depositional and diagenetic models of the field. Subsequently the GeoPODS are conditioned to the near-wellbore data and at the same time spatially-commensurate with the reservoir dynamic simulator for distributing the dynamic properties away from the wells. The following sections describe how we applied the integrated near-wellbore rock-typing and upscaling workflow to Field X.

A series of 'roadmaps' has been included to highlight the key steps of the workflow in the corresponding sub-sections.

3. Obtaining geological rock types (GeoRTs)

The specific types and distributions of the pores present within the reservoir rocks impart strong control on the production and stimulation characteristics of carbonate reservoirs (e.g. Chilingarian et al. 1992; Honarpour et al. 1992; Jodry 1992; Wardlaw 1996; Mazullo 2004; Chandra et al. 2015). It is often the case that the types of fabric-selective pores coincide with the depositional environment of the rock (Hollis et al. 2010; Van der Land et al. 2013). Understanding the crucial links between depositional and diagenetic models can provide valuable guidance towards unravelling the relationships between lithofacies and petrophysical groups (Gomes et al. 2008), and towards the evaluation of the reservoir flow properties (Mazullo 2004). Hence the prime incentive for obtaining the GeoRTs is to capture the key relationships between the depositional and diagenetic features with considerations to their impact on reservoir flow properties.

Figure 6 illustrates the integrated near-wellbore rock-typing and upscaling workflow, highlighting the steps taken to obtain GeoRTs. As discussed in the earlier sections, late-burial corrosion played a critical role in the evolution of reservoir petrophysical properties in Field X (Wright & Barnett 2011; Chandra et al. 2015). In order to obtain the GeoRTs in Field X, the lithofacies types, stylolite types and the CEP types observed in the studied wells were characterised, logged and digitised. For this we used core and thin-section data from over 300 meters of well cores from 4 vertical wells and 1 highly deviated pilot well. These core description logs were then used to divide the near-wellbore region of the wells into centimetre to decimetre scale intervals. Based on the gross depositional model, the lithofacies observed in Field X were grouped in to 6 major lithofacies in A zone and 6 in B zone. In total, Field X contains 10 main lithofacies types, with some common to both zones (see Table 1).

The two main types of stylolite distributions observed in Field X are; i) low amplitude stylolites (LAS) with low intensity of associated tension gashes and ii) high amplitude stylolites (HAS) with high intensity of associated tension gashes. The main types of CEP observed in Field X are; i) 'CEP1', representing the well intervals with high proportions of well-connected chalky microporosity and some mesoporosity, and ii) 'CEP2', which is mainly macroporosity including vuggy, moldic and leached stylolites and tension gash porosity. The factors and processes that acted as key controls on the intensity and spatial distribution of corrosion-enhanced porosity in Field X were reservoir stratigraphy, depositional setting and pressure dissolution. In the following sub-sections we discuss the main controls of burial corrosion that were considered for the classification of GeoRTs.

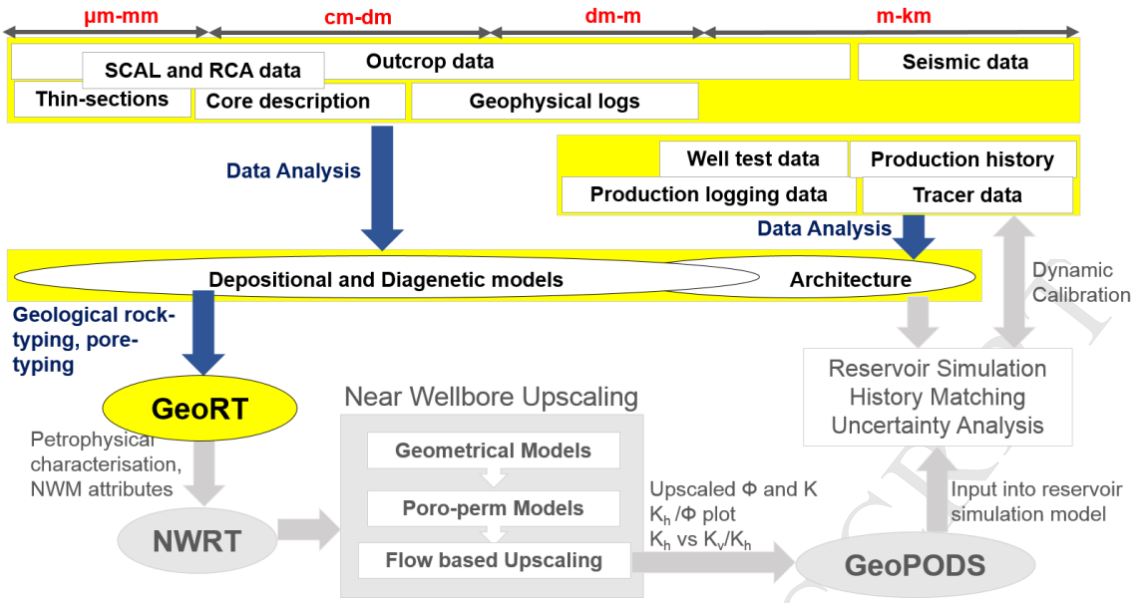

Fig. 6. Summary of the integrated near-wellbore rock-typing and upscaling workflow. A geological rock type (GeoRT) is a division of a lithofacies type that went through similar diagenetic processes. A near-wellbore rock type (NWRT) is a bin of GeoRTs that have similar petrophysical properties at core scale and near-wellbore modelling (NWM) parameters. A Geological-Porosity Derived System, (GeoPODS) is equivalent to a Global Hydraulic Element consisting of a bin of NWRTs grouped based on the upscaled porosity-permeability. The steps taken to obtain GeoRTs are highlighted here in yellow.

Table 1 Summary of major lithotypes present in A and B zones.

#	Description	Interpretation	Zone
1	Coskinolina-Grainstone	Inner ramp	**B**
2	Coskinolina-Packstone	Inner ramp	**B**
3	Coskinolina Hash- Packstone /Wackestone	Shallow mid ramp	**B**
4	Framestone with platy corals	Shallow mid ramp	**B**
5	Floatstone with platy corals	Shallow Mid ramp	**B, A**
6	Rotalids- packstone	Mid ramp	**B, A**
7	Nummulitides- Packstone	Outer ramp	**A**
8	Nummulitides- Grainstone /Wackestone	Outer ramp	**A**
9	Nummulitides- Wackestone /Packstone	Outer ramp	**A**
10	Shale zones	unconformities	**A**

3.1. Main controls of late-burial corrosion at reservoir scale

At the regional scale, the East-fault zone and the A/B Supra-unconformity shale seem to have played a critical role in the distributions of corrosion-enhanced porosity (CEP) in A Zone and B Zone. Seismic data suggest that Field X comprises extensive breccia pipes and collapse features (Figure 7b) that are hundreds of meters in diameter, and which appear to be associated with the NNW-SSE trending strike-slip fault system. Based on this and earlier geological interpretations, it is hypothesised that the East-fault zone was probably one of the main conduits of the late-burial corrosion fluids to enter Field X (Figure 7a). Hence it is expected to see an increasing trend in the intensity of corrosion of the reservoir formation closer to this fault zone. Statistical analysis of the digitised CEP logs from the studied wells suggests a good correlation between the distance of wells from the fault zone and the

percent of CEP2 type porosity, which is associated with high intensity of burial corrosion (Figure 7c). It must be noted that although the breccia pipes can act as major vertical permeability enhancers, these were not included in the reservoir model built by the operator since they were outside the reservoir model boundaries. This is because the breccia pipes are associated with the East Fault Zone, which was one of the boundaries of the reservoir model. On the other hand, the A/B Supra-unconformity shale (Figure 7a) probably acted as an aquitard, causing the burial derived corrosive fluids to concentrate in the matrix of B Zone, resulting in more intense corrosion. This is evidenced by the significantly higher proportions of CEP2 type porosity in B Zone (Figure 8a), characterised by high proportions of leached macroporosity caused by advanced and intense corrosion. This hypothesis is also favoured by the field production data and tracer data, which suggest that B Zone acts as a stratified high permeability zone of much higher reservoir rock quality than A Zone. This inference is supplemented by the comparison of porosity-permeability values (Figure 8b) and pore-size distributions (Figure 8c) between A Zone and B Zone. Overall, A Zone has a lower rock quality index and lower pore-size range compared to B Zone.

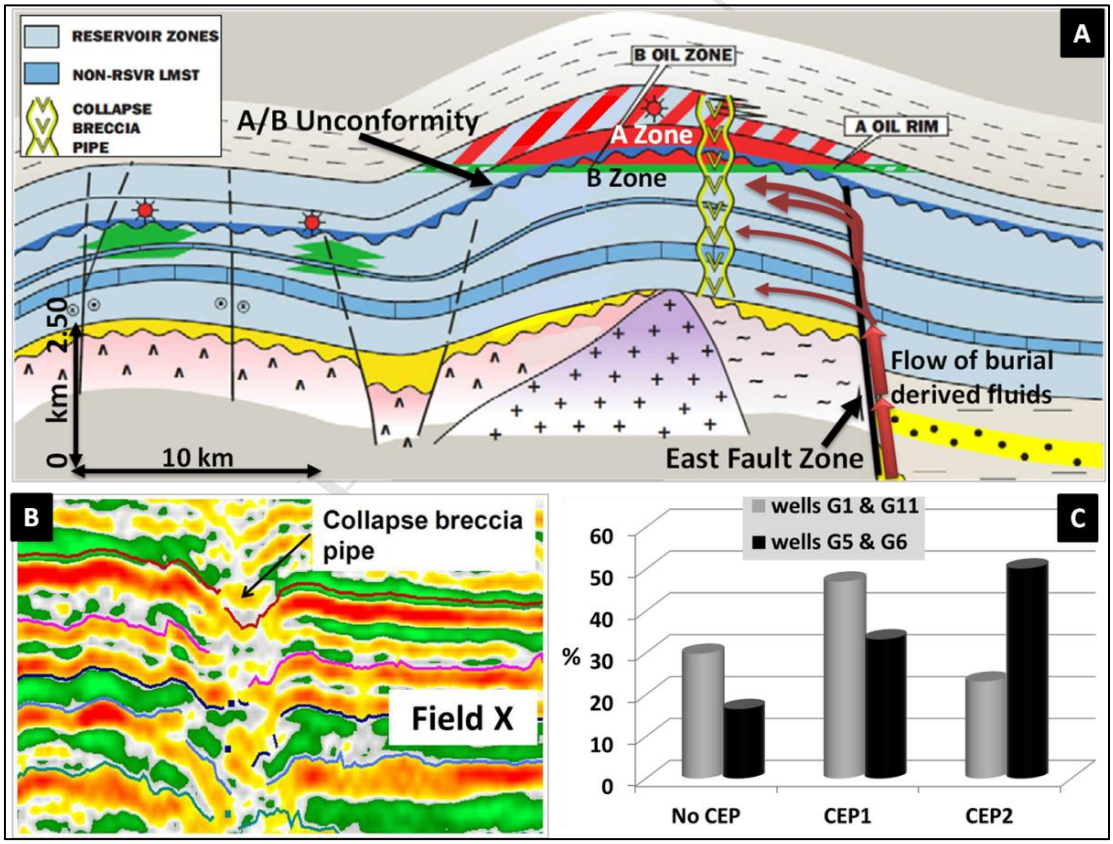

Fig. 7. (**a**) Idealised cross-section of Field X illustrating the East fault zone, the A/B Supra-unconformity shale and the flow of burial derived fluids into the reservoir formation through the fault zone. (**b**) Collapse breccia pipe associated with the East fault zone observed on seismic data. (**c**) Histogram of cumulative percentages of CEP types in the studied wells. Wells G5 and G6, which are closer to the East fault zone compared to wells G1 and G11, show higher percentage of CEP2. CEP2 is characterised by high proportions of leached macroporosity caused by advanced and intense corrosion.

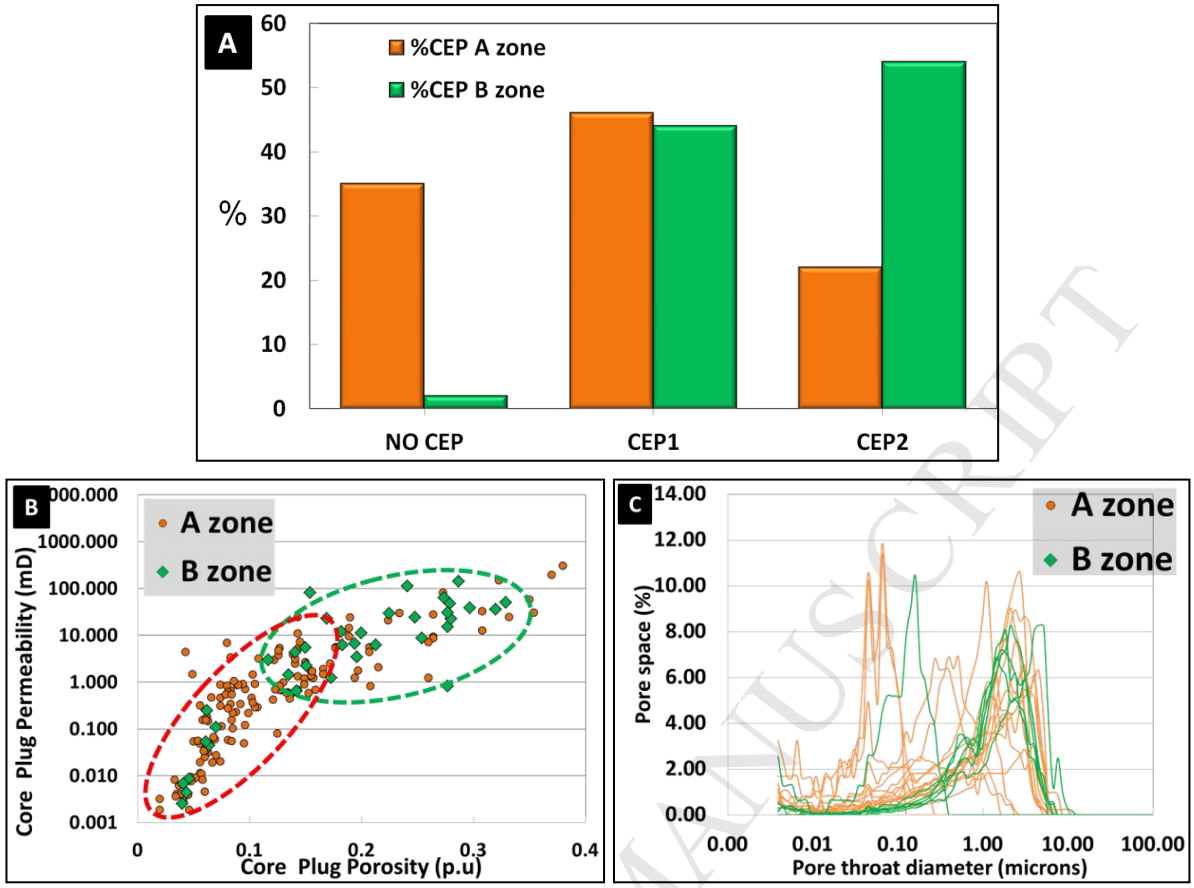

Fig. 8. (**a**) Histogram of cumulative percentage of corrosion-enhanced porosity (CEP) types showing higher proportions of CEP2 type porosity in B Zone. (**b**) Cross-plot showing higher porosity-permeability values in B Zone compared to A Zone. (**c**) Plot of pore size distributions demonstrating higher pore size distributions in B Zone compared to A Zone.

3.2. Main controls of late-burial corrosion at sub-grid scale

Core and thin-section data suggest a strong correlation between the distribution and types of stylolites and the development of CEP at centimetre to decimetre scale (Figure 9a and b). A vast majority of the stylolites and tension gashes are associated with halos of moderately to highly corroded CEP zones that are highly permeable, as observed from the mini-permeameter measurements. This supports the hypothesis that stylolites acted as conduits to the flow of the corrosive fluids into the surrounding matrix during the late-burial corrosion phase in Field X (Wright & Barnett 2011). Figure 10a illustrates the role of stylolites in the distribution of corrosion-enhanced porosity in the adjacent reservoir formation. Figure 10b illustrates the links between the depositional and diagenetic processes in Field X at core scale. The distribution of stylolite types is strongly related to the lithofacies distribution in the reservoir zones. Stylolitisation was relatively low in the outer ramp Nummulitic packstones and wackstones of A Zone due to higher clay content. A Zone mainly consists LAS type stylolites and comprises a much lower percentage of CEP2 type porosity compared to B Zone (Figure 8a). The millimetre-sized clay seams and microstylolites in A Zone caused only low to moderately intense corrosion, which resulted in widespread microporosity development in these formerly tight

cemented limestones. In contrast, B Zone is dominated by inner ramp Coskinolina grainstones and developed high amplitude stylolites and associated tension gashes. The HAS type stylolites in B Zone allowed the corrosive fluids to selectively remove the fine grained walls of agglutinated miliolid foraminiferas in the early phase of corrosion. At a more advanced stage, the sparite and more coarsely crystalline foraminiferas were extensively corroded. Hence, B Zone, which is predominated by HAS and LAS type stylolites, contains higher percentages of CEP1 and CEP2 compared to A Zone. This contrast in distribution of porosity types in B Zone and A Zone could have also been amplified by the effect the of A/B Supra-unconformity shale as discussed before.

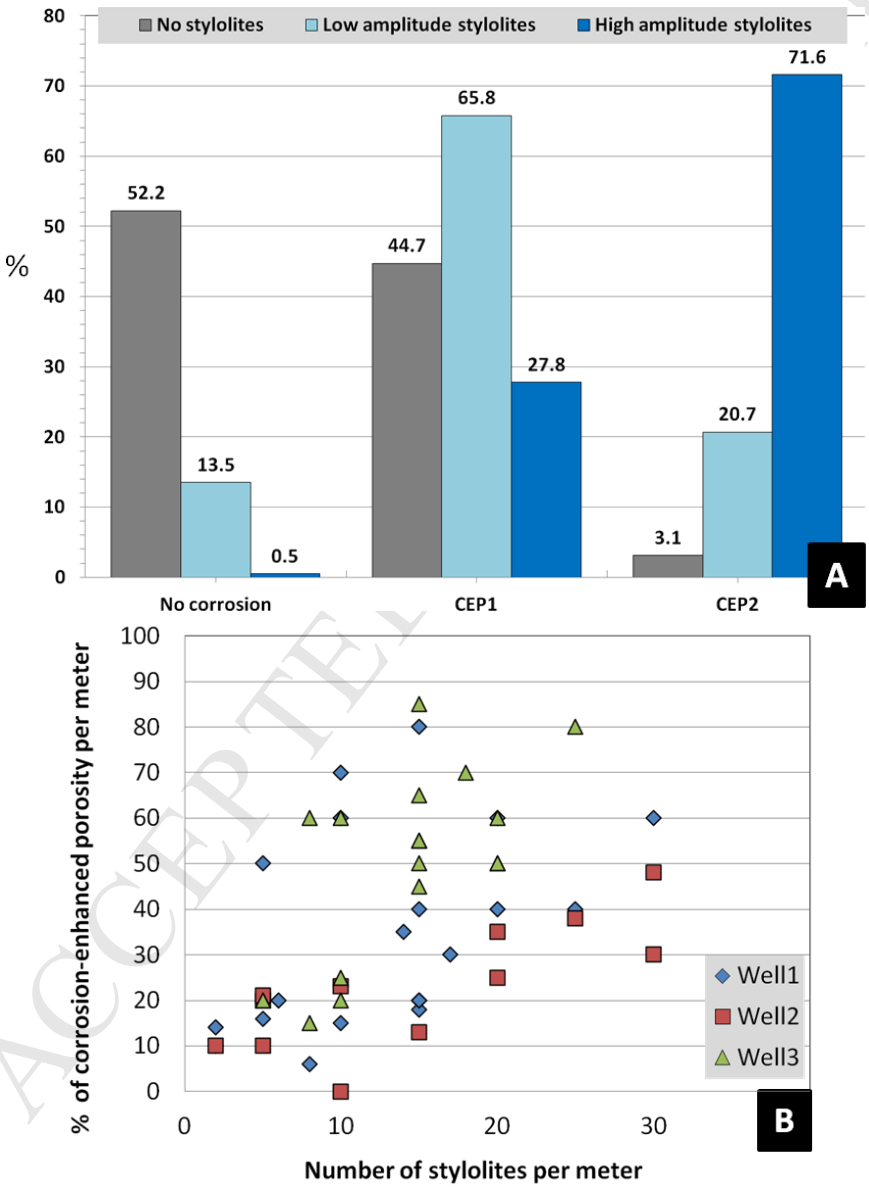

Fig. 9. (**a**) Histogram illustrating the percent of corrosion-enhanced porosity types associated with the various stylolite types in Field X. The high amplitude stylolites are associated with higher amounts of CEP2, characterised by high amounts of leached macroporosity. (**b**) Correlation between percentage of corrosion-enhanced porosity per meter and number of stylolites per meter for the studied wells. The extent of corrosion increased with the number of stylolites per meter.

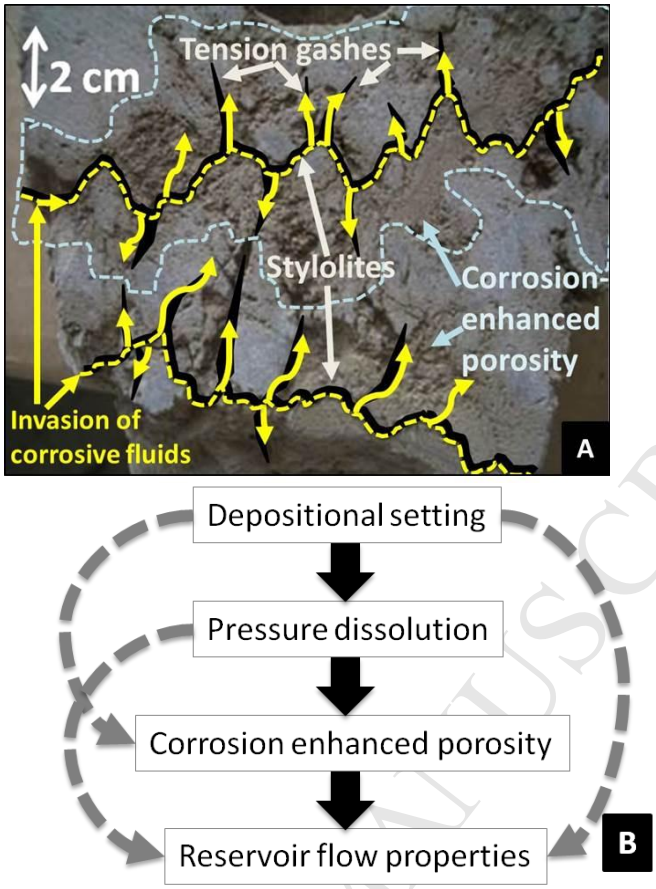

Fig. 10. (**a**) Illustration of stylolites and tension gashes acting as conduits to the flow of the corrosive fluids into the surrounding matrix. (**b**) Illustration of the main controls of reservoir properties at core-scale and the links established between the lithofacies types, stylolite types and extent of corrosion-enhanced porosity in Field X.

3.3. Field X GeoRTs

Overall, 16 GeoRTs in A Zone and 16 in B Zone were identified based on the relationships observed between the main lithotypes, presence of leached stylolites and associated tension gashes, and the extent of matrix microporosity and macroporosity (Table 2). The GeoRT logs obtained with the help of core and thin-section descriptions were used to divide the near-wellbore region of the wells into centimetre to decimetre scale intervals. The next section describes how these GeoRTs were further grouped into NWRTs based on petrophysical analysis.

354 **Table 2.** Summary of GeoRTs present in A Zone and B zone.

GeoRT A Zone	Description	GeoRT B Zone	Description
GeoRT A 1	Shale	GeoRT B **1**	Inner ramp Coskinolia grainstone with CEP1
GeoRT A 2	Mid-ramp Rotalid packstone	GeoRT B **2**	Inner ramp Coskinolia packstone with CEP1
GeoRT A 3	Outer ramp Nummulitide packstone	GeoRT B **3**	Shallow mid-ramp Coskinolina Hash packstone-wackstone with CEP1
GeoRT A 4	Outer ramp Nummulite wackestone-packstone	GeoRT B **4**	Mid-ramp-Rotalid-Packstone with CEP1
GeoRT A 5	Shallow mid-ramp floatstone with platy corals	GeoRT B **5**	Inner-ramp Coskinolina grainstone with CEP1 and LAS
GeoRT A 6	Shallow mid-ramp floatstone with CEP1	GeoRT B **6**	Inner ramp Coskinolia packstone with CEP1 and LAS
GeoRT A 7	Mid-ramp Rotalid packstone with CEP1	GeoRT B **7**	Shallow mid-ramp Coskinolina Hash packstone-wackstone with CEP1 and LAS
GeoRT A 8	Outer ramp Nummulitide packstone with CEP1	GeoRT B **8**	Shallow mid ramp framestone with LAS and CEP1
GeoRT A 9	Outer ramp Nummulite wackestone-packstone with CEP1	GeoRT B **9**	Shallow mid ramp floatstone with LAS and CEP1
GeoRT A 10	Shallow mid-ramp floatstone with LAS and CEP1	GeoRT B **10**	Mid-ramp Rotalid packstone with LAS and CEP1
GeoRT A 11	Mid-ramp Rotalid packstone with LAS and CEP1	GeoRT B **11**	Inner ramp Coskinolia grainstone with HAS and CEP2
GeoRT A 12	Outer ramp Nummulitide packstone with LAS and CEP1	GeoRT B **12**	Inner ramp Coskinolia packstone with HAS and CEP2
GeoRT A 13	Outer ramp Nummulite grainstone-wackestone with LAS and CEP1	GeoRT B **13**	Shallow mid-ramp Coskinolina Hash packstone-wackstone with HAS and CEP2
GeoRT A 14	Outer ramp Nummulite wackestone-packstone with LAS and CEP1	GeoRT B **14**	Shallow mid ramp framestone with HAS and CEP2
GeoRT A 15	Shallow mid-ramp floatstone with HAS and CEP2	GeoRT B **15**	Shallow mid ramp floatstone with HAS and CEP2
GeoRT A 16	Outer ramp Nummulite grainstone-wackestone with HAS and CEP2	GeoRT B **16**	Mid-ramp Rotalid packstone with HAS and CEP2

LAS = Low amplitude stylolites
HAS= High amplitude stylolites
CEP1= Corrosion-enhanced micro- and mesoporosity
CEP2= Corrosion-enhanced macroporosity including leached stylolites and tension gashes

355 # 4. Near-wellbore upscaling of GeoRTs for reservoir simulation

356 The GeoRTs represent the geological-petrophysical heterogeneity of the reservoir rock at the pore and
357 core scale. This scale is well below the practical size of a reservoir simulation grid-block. It is hence
358 necessary to efficiently upscale the GeoRTs to the field scale so that they can be used in reservoir
359 simulation studies. Chandra et al. (2013a & c) demonstrated that NWM can effectively capture and

upscale centimetre to decimetre scale geological features in large reservoir simulation models and improves the dynamic calibration of geomodels. Near-wellbore models were generated by recreating the sedimentary processes using a process-oriented modelling approach (Wen et al. 1998; Nordahl et al. 2005). Process-oriented modelling approach formulate deterministic geological processes such as migration and deposition of sedimentological components in a stochastic framework (e.g. Nordahl 2004; Elfenbein et al. 2005). The depositional structures were 'overprinted' with the appropriate diagenetic features in these models using an object modelling function (Chandra et al. 2013c; Dabek & Knepp 2011). The resulting geometrical models were populated with porosity and permeability values. Flow-based upscaling was used to obtain effective porosity and permeability distributions at reservoir simulation grid-block scale. To facilitate the input of the GeoRTs into near-wellbore upscaling, they were further grouped into NWRTs. This was based on petrophysical characterisation of the GeoRTs using RCA and SCAL data and with consideration to the geometrical modelling aspects of the associated sub-grid scale heterogeneities. For instance, the presence of high proportions of leached high-amplitude stylolites could strongly influence the effective flow properties of the simulation grid-block. Hence, these stylolites were modelled explicitly using the appropriate geometrical and petrophysical descriptors in the near-wellbore upscaling software. Figure 11 illustrates the integrated near-wellbore rock-typing and upscaling workflow, highlighting the steps taken to obtain NWRTs.

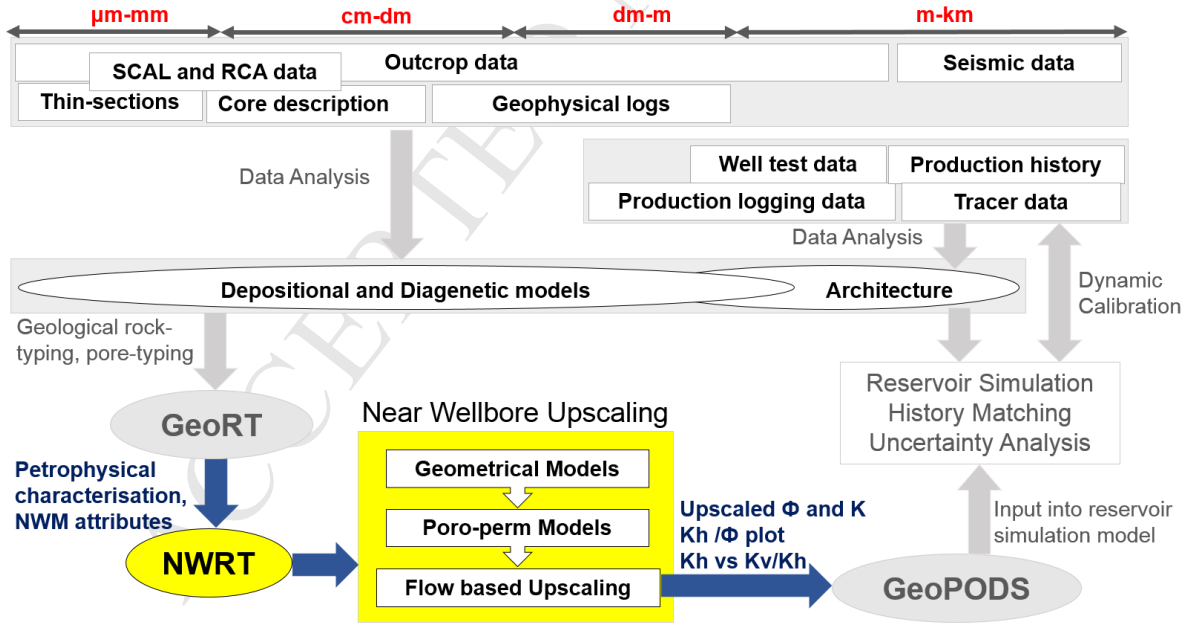

Fig. 11. Summary of the integrated near-wellbore rock-typing and upscaling workflow highlighting the steps taken to obtain Near-Wellbore Rock Types (NWRTs) from GeoRTs, and modelling and upscaling them using NWU tools.

4.1. Porosity and permeability characterisation of GeoRTs

The GeoRT logs from the near-wellbore regions were used in conjunction with the core plug and probepermeameter data to estimate porosity and permeability of the GeoRTs in the studied wells. As mentioned before, the available core plug data suffers from sample insufficiency due to poor core recovery of the well intervals containing GeoRTs with high proportion of CEP types. This is because the reservoir rock was mechanically weak as it was strongly altered by corrosive fluids. This resulted in a sample bias of RCA and SCAL data towards the GeoRTs that mainly contained the uncorroded lithofacies. However, probepermeameter measurements supplemented the core plug data and provided an estimate of the upper and lower bounds of the permeability range. The uncertainties associated with the probepermeameter data (Corbett et al. 1999) and the issues related to the measurement of stylolite and tension gash porosity-permeability were discussed by Chandra et al. (2015). Based on probepermeameter and core plug data, the GeoRTs were binned into 7 porosity-permeability groups in A Zone and 7 in B Zone (Table 3). The range of probepermeameter measurements and the porosity-permeability cross-plots of the porosity-permeability groups are shown in (Figure 12).

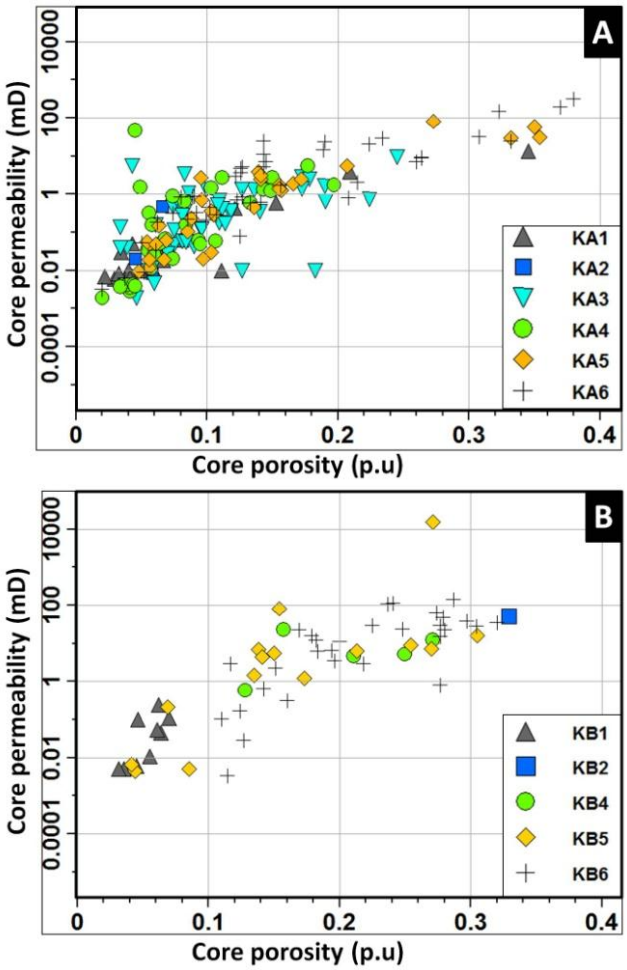

Fig. 12. Porosity-permeability cross-plots for the porosity-permeability groups from (**a**) A Zone and (**b**) B Zone. Groups K-A1 and K-B1 (Table 3), containing no or low presence of any CEP types, show much lower porosity-permeability compared to groups K-A6 and K-B6 (Table 3) that represent vuggy and moldic macroporosity.

Due to the highly heterogeneous distribution of the CEP types, even at the core scale, a wide range of porosity-permeability values were obtained for the GeoRTs. Nevertheless, there was a visible trend of increasing porosity-permeability values that correlate to the increase in intensity of late-burial corrosion. Overall, groups K-A6 and K-B6 (Table 3) show the highest porosity-permeability range in A Zone and B Zone respectively (Figure 12). These groups constitute the GeoRTs with higher proportion of CEP2 type porosity, i.e. vuggy and moldic macroporosity associated with leached stylolites and tension gashes. Groups K-A1 from A Zone and K-B1 from B Zone (Table 3), containing GeoRTs with no or low presence of any CEP types recorded much lower porosity-permeability range (Figure 12).

Table 3. Porosity-permeability groups in A Zone and B Zone. See Table 2 for GeoRT descriptions.

A Zone		B Zone	
GeoRT	**Porosity-permeability Group**	**GeoRT**	**Porosity-permeability Group**
1	K-0	-	-
2,3,4,5	K-A1	4, 10	K-B1
7	K-A2	8	K-B2
6, 8, 11, 12	K-A3	16	K-B3
10, 9	K-A4	1, 2, 3, 7	K-B4
13, 14	K-A5	5,6, 9, 12	K-B5
15, 16	K-A6	11, 13, 14, 15	K-B6

4.2. GeoRT capillary pressure characteristics

Capillary pressure (P_c) data provides information about pore throat diameters, pore connectivity and their impact on fluid flow in the reservoir (Bear 1972). With respect to reservoir simulation, the applications of P_c curves are mainly two-fold. First, P_c curves are used to distribute the initial saturations in the reservoir simulation gridblocks during initialisation of the simulation model. Second, P_c curves contribute to the fluid-flow equations in the form of gradients of the phase pressures (e.g. Fanchi 2006) that transfer oil between low and high permeability regions during imbibition (Schmid & Geiger 2013). The former is one of the most crucial contributors to the initial hydrocarbons-in-place calculations in the reservoir simulation model. In order to ensure that the GeoRTs reflect the dynamic effects of capillary pressure, they were reconciled with the Mercury Injection-Capillary Pressure (MICP) data provided by the operator. MICP data from 22 samples were used for this study. The GeoRTs corresponding to high proportion of corrosion-enhanced porosity (See Table 2) displayed low threshold entry pressures of less than 2.25 psia. In contrast, the GeoRTs associated with no or low corrosion (See Table 2) displayed threshold entry pressures higher than 100 psia. The GeoRTs associated with tight matrix (See Table 2) without any corrosion-enhanced porosity displayed high initial water saturation values and steep saturation-height curves. The GeoRTs with CEP1 type porosity displayed higher initial saturation values compared to those GeoRTs that contain CEP2. The former GeoRTs were abundantly present in the A Zone and represent intermediate quality

rock with patchy microporosity grading into larger meso-pores. The GeoRTs with CEP2 type porosity generally represented the best quality rock in the reservoir and were dominated by macro-pores. These GeoRTs were abundantly present in the B Zone and characterised by broadly shaped saturation curves and low initial water saturation values. Consequently, the saturation-height functions were broadly classified into three main groups based on the corrosion-enhanced porosity of the GeoRTs. The saturation-height function curves corresponding to GeoRTs with tight matrix without any corrosion-enhanced porosity types and GeoRTs with CEP1 and CEP2 are shown in Figure 13.

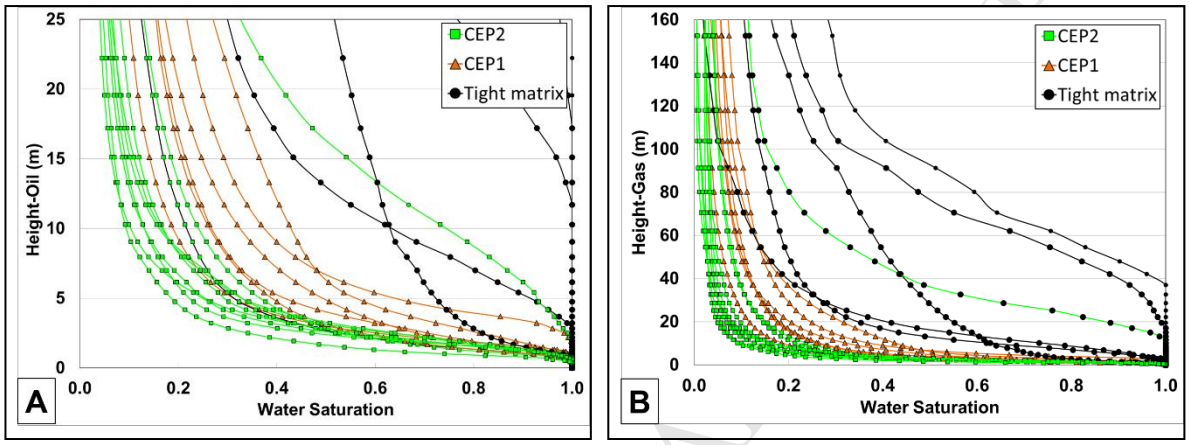

Fig. 13. Three main groups of GeoRTs in Field X based on saturation-height functions, corresponding to tight matrix and corrosion-enhanced porosity types CEP1 and CEP2.

4.3. Relative permeability characterisation of GeoRTs

The relative permeability characteristics of reservoir rock types, in particular the saturation and relative permeability end-points, are fundamentally important for reliable estimation of ultimate hydrocarbon recovery (Dykstra & Parsons 1950; Buckley and Leverett, 1952). Unsteady state water-oil and gas-oil relative permeability analysis results at 2000 psi and 70 ºF provided by the operator were used in this study. Figure 14 shows the groups of relative permeability curves of the GeoRTs based on corrosion-enhanced porosity types CEP1 and CEP2. Initial water saturations and the water relative permeability at critical oil saturation suggest that the GeoRTs with high proportion of CEP1 could be strongly water-wet. In contrast, the GeoRTs with high proportion of CEP2 tend to be intermediate-wet to weakly oil-wet. It was observed that the critical oil saturation values of the GeoRTs tend to decrease with the increase in the proportion of CEP2 type porosity. The residual oil saturation varied between 0.19-0.36 for the samples from the B Zone, in which the oil rim is located. The initial water saturation varied between 0.17-0.47 for the samples from the A Zone and 0.37-0.308 for those from the B Zone. The cross point of the water-oil relative permeability curves occurred at less than 50% water saturation for over 95% of the SCAL samples. The water relative permeability at maximum water saturation ranged from 0.30 up to 0.70 in A Zone and from 0.13 to 0.41 in B Zone.

It is challenging to characterise each GeoRT with its own set of relative permeability curves due to the limited availability of SCAL data samples. Nevertheless, we were able to obtain some general

inferences regarding the potential relationship between the extent of late-burial corrosion and the relative permeability characteristics of the GeoRTs. It appears that the samples from the wells that are located away from the East-fault zone (Wells G11 and G1) tend to be more water-wet compared to wells which are located closer to the fault zone (Wells G6 and G5) (Figure 2b). This trend could be associated with the role of the East-fault zone in the distribution of corrosion-enhanced porosity in Field X, causing higher proportions of CEP2 type porosity in the regions closer to the fault zone compared to the flank of the reservoir.

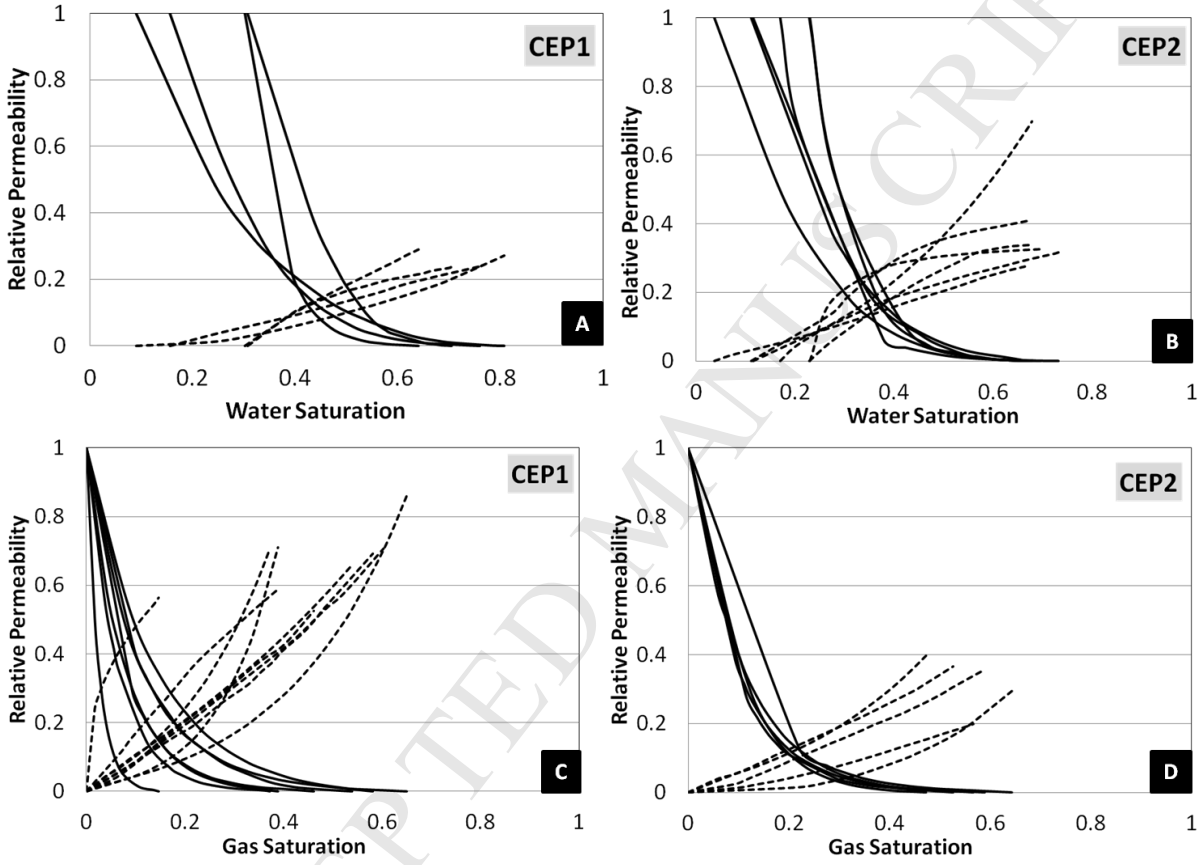

Fig. 14. Groups of water-oil and gas-oil relative permeability curves of the GeoRTs based on the corrosion-enhanced porosity types CEP1 and CEP2.

4.4. Near-wellbore upscaling of GeoRTs

Based on the petrophysical analysis discussed in the previous sections and the associated NWM parameters, the GeoRTs were grouped into 7 NWRTs in A Zone (Table 4) and 7 in B Zone (Table 5). The NWM aspects considered for the grouping of GeoRTs are listed in Tables 4 and 5. The NWRTs were then modelled using the object modelling feature in the NWM software, SBED^{TM} (Chandra et al. 2013c; Chandra 2014). The geometries of near-wellbore models in this study were typically 20 cm x 20 cm x 20 cm in size. The main input required for NWM were the spatial and geometrical parameters and the statistics of the petrophysical properties associated with the corresponding GeoRTs. As an example, Figure 15a illustrates the 'network rod' object model template in SBED^{TM}, which was used for modelling the NWRTs containing CEP types with micro- and macro-porosity. Table 6 summarises

480 the geometrical parameters applied to the network model template. In the NWRT scenarios with
481 stylolite and tension gashes, various geometrical and spatial distribution aspects of leached stylolites
482 and associated tension gashes were superimposed on the background matrix. The stylolites were
483 explicitly modelled by applying a standard deviation of 1 to the roughness of the horizontal layers of
484 the geometrical model (Chandra 2014). Figure 15b illustrates the 'U-shaped body' object model
485 template in SBED™ that was used for modelling tension gashes.

486 **Table 4.** Summary of NWRTs present in A Zone. See Table 2 for GeoRT descriptions.

#	NWRT	GeoRT A Zone	Porosity-permeability group	Saturation-height group (Figure 13)	Near-wellbore modelling aspects
0	NWRT-A0	1	K-A0	-	Shale lamina
1	NWRT-A1	2,3,4,5	K-A1	Tight matrix	Tight matrix, multiple porosity-permeability scenarios
2	NWRT-A2	7	K-A2	CEP1	Multiple realisations of K-A2 overprinted on tight matrix
3	NWRT-A3	6, 8, 11, 12	K-A3	CEP1	Multiple realisations of K-A3 overprinted on tight matrix
4	NWRT-A4	10, 9	K-A4	CEP1	Multiple realisations of K-A4 overprinted on KA3
5	NWRT-A5	13, 14	K-A5	CEP2	Multiple realisations of K-A5 overprinted on KA3
6	NWRT-A6	15, 16	K-A6	CEP2	Multiple realisations of K-A5, explicitly modelled leached stylolites and tension gashes overprinted on KA3

487 **Table 5.** Summary of NWRTs present in B Zone. See Table 2 for GeoRT descriptions.

#	NWRT	GeoRT B Zone	Porosity-permeability group	Saturation-height group (Figure 13)	Near-wellbore modelling aspects
0	NWRT-B0	1	K-B0	-	Shale lamina
1	NWRT-B1	4, 10	K-B1	Tight matrix	Multiple realisations of of KB1 overprinted on tight matrix
2	NWRT-B2	8	K-B2	CEP1	Multiple realisations of of KB2 overprinted on tight matrix
3	NWRT-B3	16	K-B3	CEP1	Multiple realisations of KB4 overprinted on tight matrix
4	NWRT-B4	1, 2, 3, 7	K-B4	CEP1	Multiple realisations of KB4 overprinted on KB3
5	NWRT-B5	5,6, 9, 12	K-B5	CEP2	Multiple realisations of K-B5, explicitly modelled leached stylolites and tension gashes overprinted on KB4
6	NWRT-B6	11, 13, 14, 15	K-B6	CEP2	Multiple realisations of K-B6, explicitly modelled leached stylolites and tension gashes overprinted on KB4

488 Core description suggested that the tension gashes were up to 6 mm wide, few mm to several
489 centimetres long and were oriented vertically to sub-vertically, originating from the mechanical
490 discontinuity along the stylolite surfaces and developed nearly parallel to the direction of vertical

stress (Chandra 2014). Figure 16 illustrates exemplary SBED^{TM} model realisations with varying spatial distributions and orientations of the tension gashes. Two cases of tension gash lengths were tested using a constant height of 2 mm. In the first case, the lengths varied from 1 cm to 5cm and in the second case from 3 cm up to 10 cm. Since the tension gashes observed on the core were oriented vertically to sub-vertically, the dip angle was varied from 0^o to 10^o (Table 6). The azimuth, i.e. orientation of the tension gashes with respect to the x-y plane, was varied from 0^o to 90^o (Table 6). The spatial distribution of the tension gashes was controlled in SBED^{TM} by defining the number of tension gashes that are randomly distributed in the NWM. In this example, two cases of tension gash distributions were tested. The first case contained 100 tension gashes per cubic metre and the second case contained 200 tension gashes per cubic metre. The former and the latter represented low density of tension gashes and high density of tension gashes, respectively.

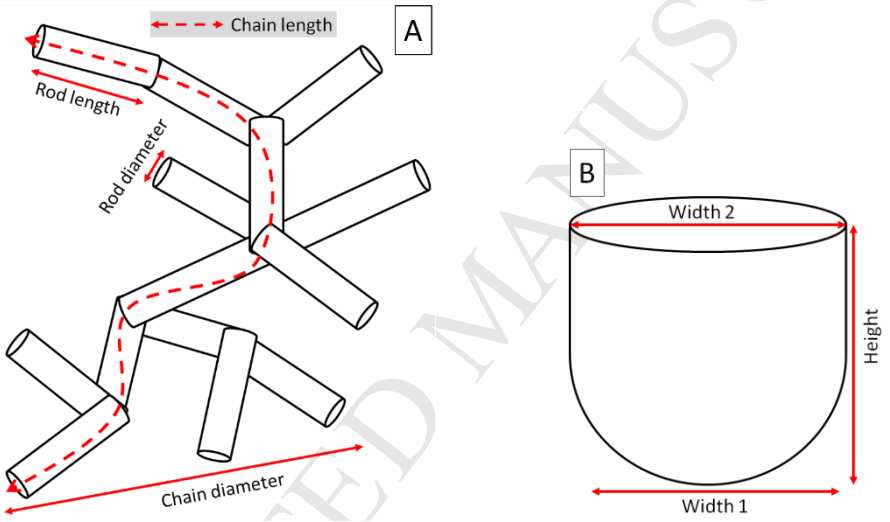

Fig. 15. (a) The 'network rod' object template in SBED^{TM} used for modelling NWRTs with CEP types containing micro- and macro-porosity. (b) The 'U-shaped body' object template in SBED^{TM} used for modelling NWRTs with leached tension gashes.

Table 6. Geometrical parameters used for modelling the corrosion-enhanced matrix porosity using the network rod and U-shaped body templates.

Shape	Parameter	Mean	Standard Deviation
Network rod	Azimuth (degree)	0.00	30.00
	Dip (degree)	0.00	30.00
	Rod length (cm)	3.00	1.00
	Chain length (cm)	10.00	2.00
	Rod diameter (cm)	3.00	0.00
	Chain diameter (cm)	2.00	0.00
U-shaped body	Azimuth (degree)	0.00	90
	Dip (degree)	0.00	10
	Width 1 (cm)	1	1
	Width 2 (cm)	1	1
	Height (cm)	0.1	0.00

The resulting centimetre-decimetre scale near-wellbore geological models were aimed to be realistic representations of the geometries and distributions of the core-scale geological features corresponding to the GeoRTs, for example the CEP types with the leached stylolites and tension gashes. Multiple stochastic realizations of high resolution porosity and permeability grids were produced for each NWRT scenario using the mean, standard deviation, minimum and maximum values of porosity-permeability distributions within each of the NWRTs. Thus, the numerous geometrical and petrophysical realisations of the NWRTs were available to capture the extremes of the geological-petrophysical heterogeneities in Field X that were observed from well data. The high-resolution NWRTs at the core scale were then upscaled to the reservoir scale using single-phase flow based upscaling to obtain the effective porosity and permeabilities of each NWRT realisation (Figure 17). This yielded the upscaled porosity-permeability and K_v/K_h distributions for the NWRTs, conditioned to the near-wellbore region. Further details of single-phase flow based upscaling in SBED™ are discussed by Chandra (2014) and references therein.

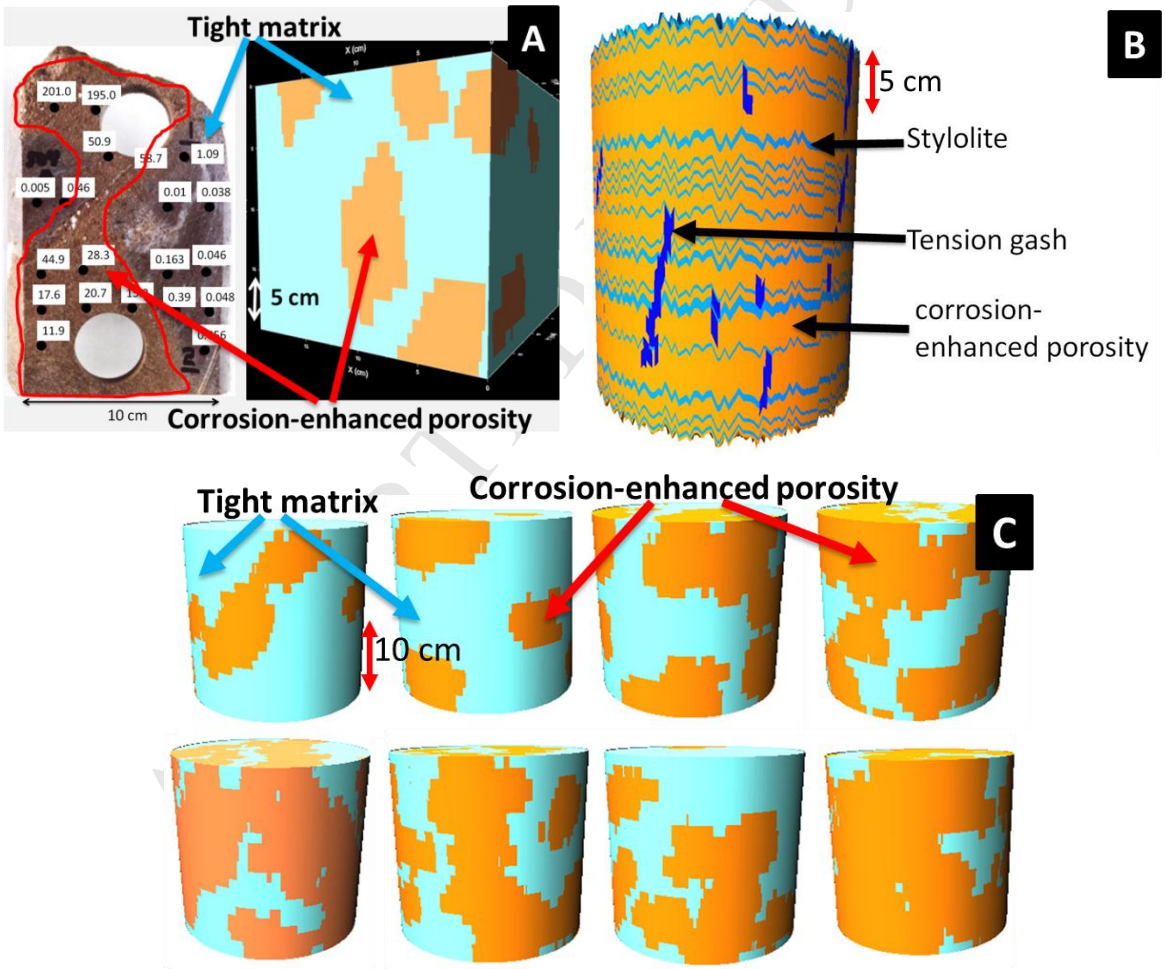

Fig. 16. (**a**) Near-wellbore model representing distribution of corrosion-enhanced porosity surrounded by a tight matrix (**b**) Example of a near-wellbore model when stylolites and associated tension-gashes are explicitly modelled. (**c**) Example model realisations of solution-enhanced porosity and tight matrix scenarios

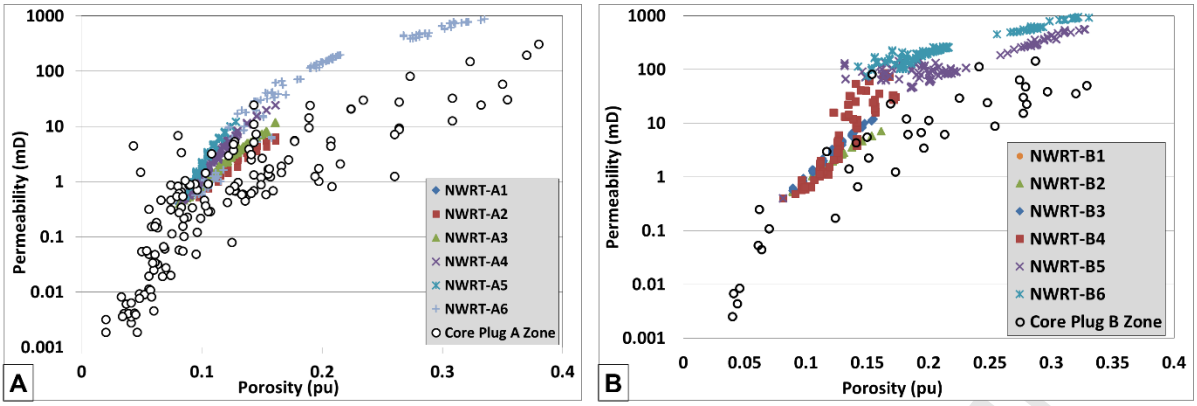

Fig. 17. Cross-plot between effective porosity and effective horizontal permeability calculated using flow-based upscaling for the various near-wellbore rock types (NWRTs) from A Zone (a) and B Zone (b). The core plug measurements have also been plotted to provide comparison between the porosity-permeability distributions in Field X before and after upscaling in both A and B Zones.

5. Geological-Porosity Derived Systems (GeoPODS)

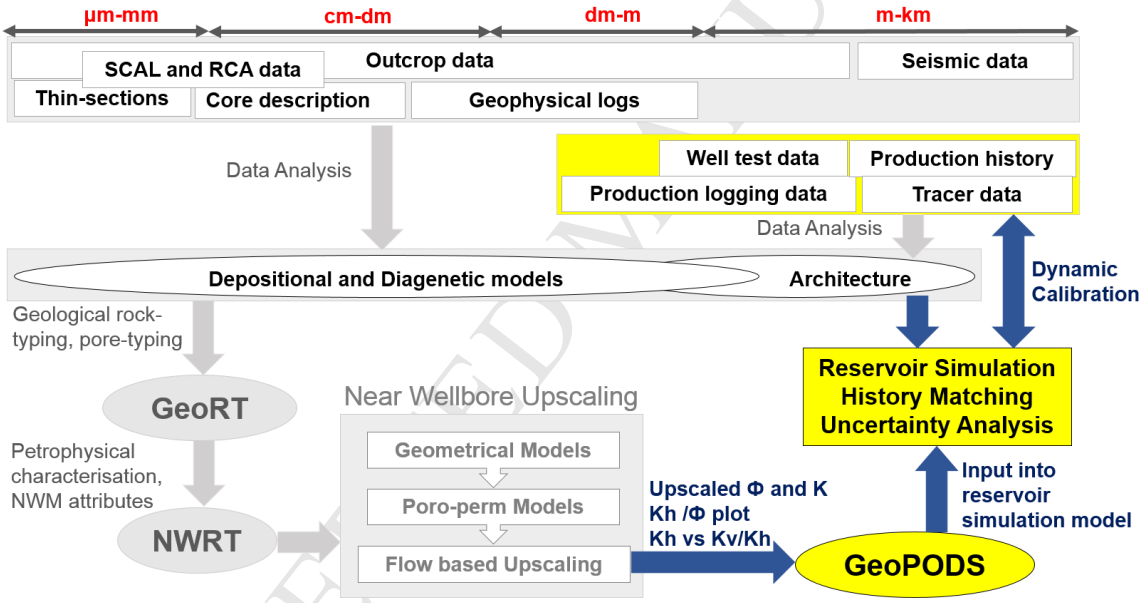

Fig. 18. Summary of the integrated near-wellbore rock-typing and upscaling workflow highlighting the steps taken to obtain Geological Porosity Derived Systems (GeoPoDS) from NWRTs and incorporating them into reservoir simulation studies.

The level of reservoir model complexity is generally case dependent, based on the objectives of the reservoir simulation study and the associated uncertainties (e.g. Fanchi 2006). Although it is computationally not possible to build reservoir simulation models using grid blocks that resolve the small scale geological features in Field X explicitly, the upscaled NWRTs from each zone (Tables 4 & 5) can be used as the reservoir rock types that preserve the small-scale and sub-grid heterogeneities in the reservoir model of Field X. However, using all NWRTs would still result in a relatively large number of rock types and Field X would comprise a total of 12 reservoir rock types, resulting from 6 NWRTs in A Zone and 6 in B Zone. As a consequence, the complexity of the reservoir modelling and

simulation workflows could increase significantly. Hence the NWRTs from both A and B Zones were further grouped into GeoPODS, i.e., the rock types from the two reservoir zones were binned into corresponding GeoPODS (see below). In effect, A and B Zones were treated together from this point. The geomodel containing GeoPODS was then used for reservoir simulation studies. Figure 18 illustrates the integrated near-wellbore rock-typing and upscaling workflow, highlighting the steps taken to obtain GeoPODS.

The predominant porosity-permeability trends of the effective porosity and permeability values resulting from near-wellbore upscaling were identified through regression analysis. The trends provided the basis for grouping the NWRTs into GeoPODS. Rather than using trends from a regression analysis, image logs could provide a more robust binning of the NWRTs at the wireline scale but such data were not available for this study. Figure 19a illustrates how GeoPODS were classified using the cross-plot obtained from near-wellbore upscaled porosity and horizontal permeability values. Overall, the NWRTs were binned into four GeoPODS in Field X: shale, G0, G1 and G2 (Figure 19a). The GeoPODS G0 mainly constituted the NWRTs derived from GeoRTs with tight matrix while G1 was dominated by NWRTs derived from GeoRTs with CEP1, i.e. corrosion-enhanced micro and meso-porosity types. The GeoPODS G2 comprises the NWRTs that correspond to GeoRTs with high CEP2, which includes leached stylolite and tension gash porosity types. The porosity-permeability values obtained from upscaling the NWRTs were used to calculate the global permeability transforms representative of each GeoPODS. The cross-plot used to obtain the correlation between near-wellbore upscaled K_v/K_h anisotropy and horizontal permeability is shown in Figure 19b. This correlation was used to calculate the vertical permeability of the GeoPODS. High and low case endmembers for the permeability transforms were also obtained for each of the GeoPODS. These endmembers were used to analyse how sample bias and incomplete porosity-permeability data at the core-scale could impact the field-scale reservoir simulation results.

To provide further comparison of our rock-types, we analysed them with respect to two common classifications schemes. Figure 19c compares the GeoPODS porosity-permeability transforms with Lucia's (1983) permeability transforms for non-vuggy carbonate fabrics. Figure 19d superimposes the GeoPODS on the 'Global Hydraulic Elements' (GHE) plot (Corbett & Potter 2004). The porosity-permeability distribution of GeoPODS G0 was coherent with Lucia's Class 3 for non-vuggy rock-fabric type and the K-transform from regression analysis corresponded to zone GHE 3. The porosity-permeability distribution of G1 was spread between Lucia's class 2 and class 3 and showed equivalence to GHE 4. G2 porosity-permeability distribution varied between Lucia's class 1 and class 2 rock fabric types and is spread across GHE 6 and GHE 5. The comparison of GeoPODS porosity-permeability relation with GHE plot corroborated the presence of three main porosity types in Field X at the reservoir grid-block scale. Table 7 summarises petrophysical attributes of the four GeoPODS of

Field X. Table 7 also lists the saturation-height function and relative permeability groups corresponding to the GeoPODS, inherited from the GeoRTs.

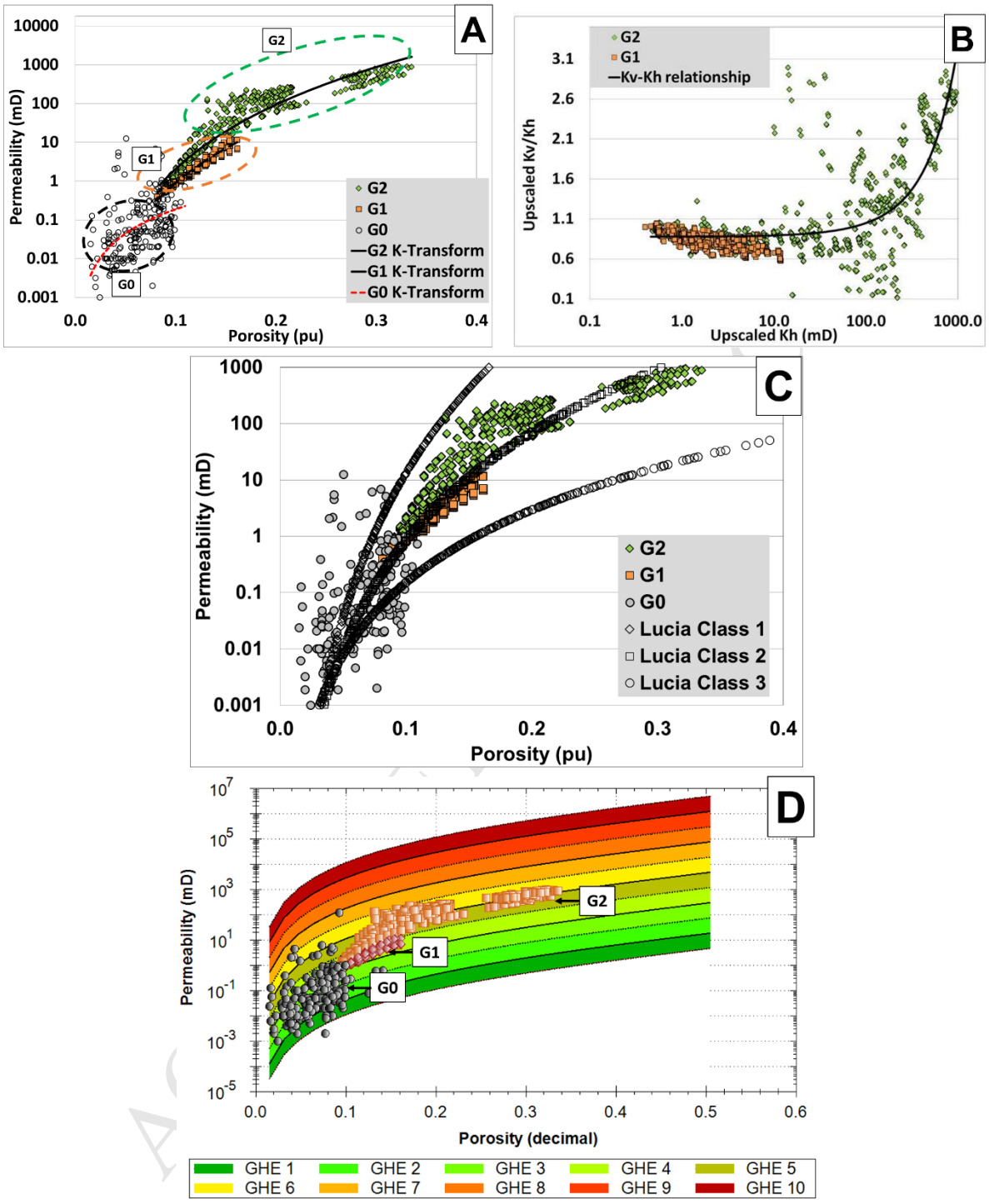

Fig. 19. (**a**) Cross-plot between effective porosity and effective horizontal permeability obtained from NWRTs and the porosity-permeability transforms used to classify GeoPODS. (**b**) Cross-plot between calculated effective horizontal permeability and effective K_v/K_h anisotropy ratio of the GeoPODS G1 and G2. (**c**) Comparison between the GeoPODS porosity-permeability crossplot and Lucia's (1983) permeability transforms for nonvuggy fabrics. (**d**) GeoPODS permeability transforms superimposed on the 'Global Hydraulic Element' (Corbett & Potter 2004) plot.

Table 7. Summary of GeoPODS and their petrophysical attributes input into reservoir simulation. Note that 'PHIE cut-offs' represent the porosity cut-offs used to populate GeoPODS in the porosity model provided by the operator.

GeoPODS	Permeability Transform	K_v/K_h anisotropy	Sw-H group	Kr group	PHIE Cut-offs
Shale	$K = 0.001$	$K_v = K_h$	CEP0	CEP0	<0.01
G0	$K = 766.42 * \Phi^{3.2229}$	$\frac{K_v}{K_h} = 8E-07 * K_h^2 + 0.0016 * K_h + 0.878$	CEP0	CEP0	[0.01, 0.05)
G1	$K = 101278 * \Phi^{5.0483}$	$\frac{K_v}{K_h} = 8E-07 * K_h^2 + 0.0016 * K_h + 0.878$	CEP1	CEP1	[0.05, 0.15)
G2	$K = 663749 * \Phi^{5.5071}$	$\frac{K_v}{K_h} = 8E-07 * K_h^2 + 0.0016 * K_h + 0.878$	CEP2	CEP2	>0.15

6. Employing GeoPODS in Field X reservoir simulation

Not only the reservoir permeability of Field X, but also the initial hydrocarbons-in-place and the critical oil saturation values are associated with high degrees of uncertainty. Due to the capillary transition zone present in the oil rim, Field X poses additional challenges for reliable characterisation and simulation of the reservoir behaviour. The unrealistic water relative permeability endpoints and local initial saturation changes applied to the original Field X geomodel to obtain history match suggest that the distribution of initial-oil-in-place and the dependency of residual oil saturation on initial water saturation require better characterisation (Chandra 2014). In order to accomplish this, we ensured that the porosity-permeability distribution, capillary pressure, and relative permeability characteristics are consistent within each GeoPODS as discussed earlier (Table 7). We next discuss the steps taken to incorporate the static and dynamic properties of the GeoPODS into the reservoir simulator.

6.1. Field X Permeability and rock quality index

Since well data from only four wells was available for this study, an entirely new scenario of Field X geomodel based on GeoPODS could not be obtained. Instead, the high resolution porosity model provided by the operator was used to distribute the GeoPODS at the reservoir grid-block scale. Since image log data was unavailable for this study, the GeoPODS were distributed in the reservoir geomodel using only porosity cut-offs. The porosity cut-offs (Table 7) for each GeoPODS were obtained by reconciling the upscaled porosity-permeability cross-plots (Figure 17) with the wireline effective porosity logs in the near-wellbore regions. These porosity cut-offs were then applied to the Field X porosity model (Figure 2b), originally supplied by the operator, to obtain the GeoPODS model. Following this, the respective permeability and K_v/K_h transforms (Table 7) were applied to the porosity model to calculate the horizontal and vertical permeability distributions within each GeoPODS in both A and B Zones. Figure 20 shows the comparison between the permeability model

derived from conventional core porosity-permeability transform and the permeability model resulting from the GeoPODS model. The reservoir rock quality index (RQI) in Field X was calculated as (Amaefule et al. 1993)

$$RQI = 0.0314\sqrt{\frac{k}{\Phi}}, \qquad (1)$$

where k is permeability and Φ is porosity. Figure 21 illustrates the comparison between the distributions of RQI in the GeoPODS case and the original geomodel. The RQI calculated for the original geomodel (Figure 21a) is significantly lower than that for the GeoPODS case (Figure 21b).

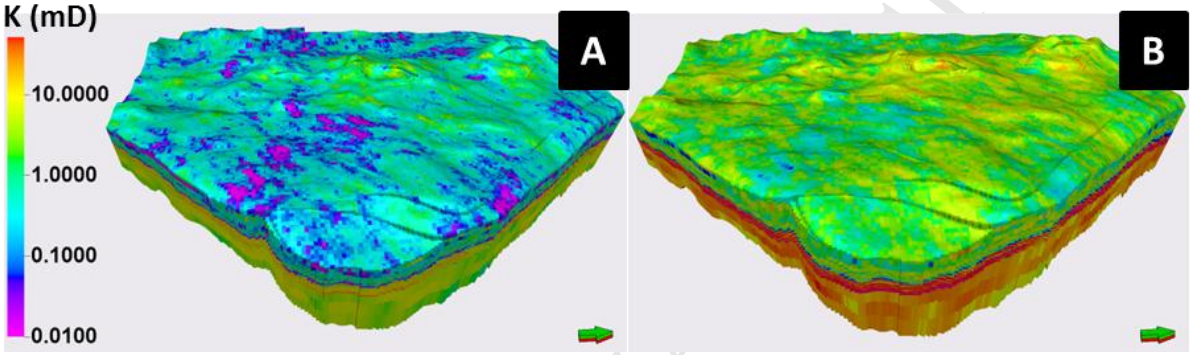

Fig. 20. (**a**) Permeability model derived from core permeability transform (**b**) Permeability model obtained from the permeability transforms of the GeoPODS.

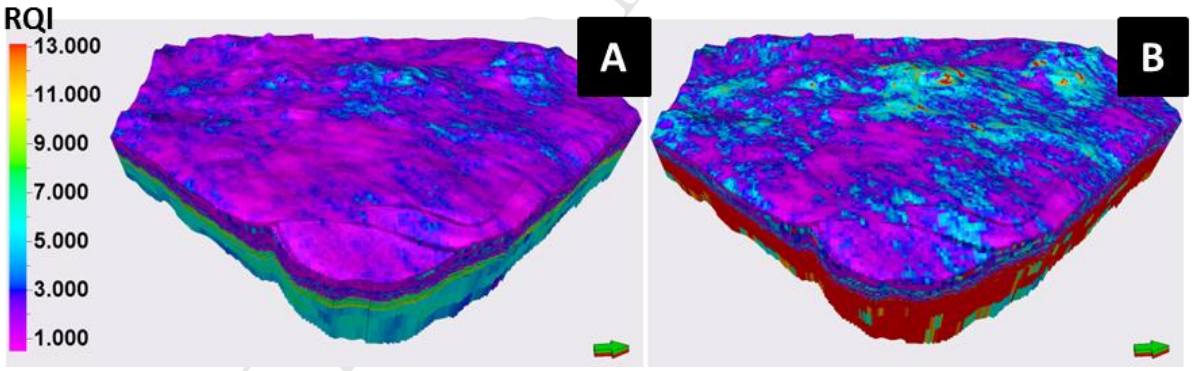

Fig. 21. (**a**) Reservoir rock quality index (RQI) distribution calculated using the permeability model derived from core permeability transform (**b**) RQI distribution calculated using the permeability model obtained from the permeability transforms of the GeoPODS. The RQI distribution in the GeoPODS case is significantly higher compared to the original geomodel, especially in the lower layers of the model that correspond to B Zone.

The RQI calculated for the GeoPODS inherently captures the enhanced flow properties caused by late-burial corrosion in Field X that could not be modelled by conventional rock-typing. In effect, the RQI distribution of the GeoPODS case implicitly represents the heterogeneity associated with micro- and macro porosity, leached stylolites and tension gashes. The characterisation of RQI in Field X hence improved due to the implementation of GeoPODS compared to the original geomodel. Furthermore, this improvement in RQI characterisation has strong implications towards the calculation of initial water saturation, and subsequently the fluids in place calculations in the

simulation model when the J-function approach is used for saturation modelling. It must be noted that the application of porosity cut-offs to populate GeoPODS in Field X geomodel relied on the basic assumption that the porosity model given by the operator is sufficiently accurate. It is hence recommended that the possible uncertainty associated with the porosity model should be given due consideration while performing a detailed history matching study.

6.2. Relative permeability curves

These relative permeability curve groups (Figure 14) were averaged and assigned to the GeoPODS. Figure 22 shows the averaged water-oil and gas-oil relative permeability curves of the GeoPODS compared with those originally used for Field X history matching. The relative permeability curves from each CEP group were averaged using the commercial software application called SCAL, which is a plug-in to the reservoir simulator ECLIPSE. The relative permeability curves were first normalised to remove the effect of the different initial water saturation values and residual oil saturation values of the samples of the same group. Then the normalised curves were averaged to obtain a single relative permeability curve, which was used as the representative of the group.

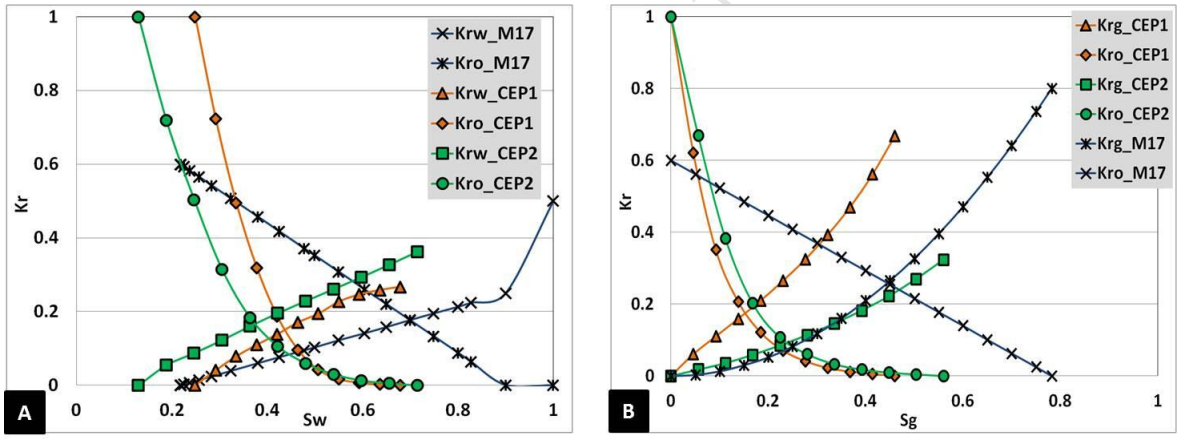

Fig. 22. (**a**) Average water-oil relative permeability curves obtained for the GeoPODS (CEP1 and CEP2) compared with those used for history matching (M17). (**b**) Average gas-oil relative permeability curves obtained for the GeoPODS (CEP1 and CEP2) compared with those used for history matching (M17).

6.3. Capillary pressure-saturation correlations

The three main groups of saturation-height functions (see Figure 13) that were obtained during the characterisation of GeoRTs in section 4.2 were used to obtain the relationship between initial water saturation and capillary pressure for the GeoPODS. As mentioned before, at this stage A and B Zones were treated together. We tested two methods to derive the relationship between capillary pressure and saturation to be implemented in reservoir simulation. In the first method we obtained a Pc-Sw correlation for each GeoPODS based on the correlation between the logarithm of capillary pressure and water saturation (Figure 23a). In the second method (Figure 23b) the relationship between J-function, P_c and water saturation was used, which is defined as

669 $$J = \frac{0.218\ P_c}{\sigma \mathrm{Cos}\,\theta} \sqrt{\frac{k}{\Phi}}. \qquad (2)$$

670 Here σ and θ are interfacial tension and contact angle between oil and water at reservoir condition,
671 respectively. These parameters have been provided by the operator. Thus, the J-function allowed us to
672 scale capillary pressure to account for the variation in porosity and permeability in the reservoir, i.e,
673 the RQI. Some of the capillary pressure curves from G0 group, which represents the poor quality
674 reservoir rock in Field X, were concave due to the micritic nature of the rock. The normalised
675 capillary pressure curve of the GeoPODS G0 (Figure 23a) could not represent this phenomenon
676 adequately. In contrast, these curves were better characterised by the J-functions (Figure 23b), which
677 account for the rock quality index of the GeoPODS.

678

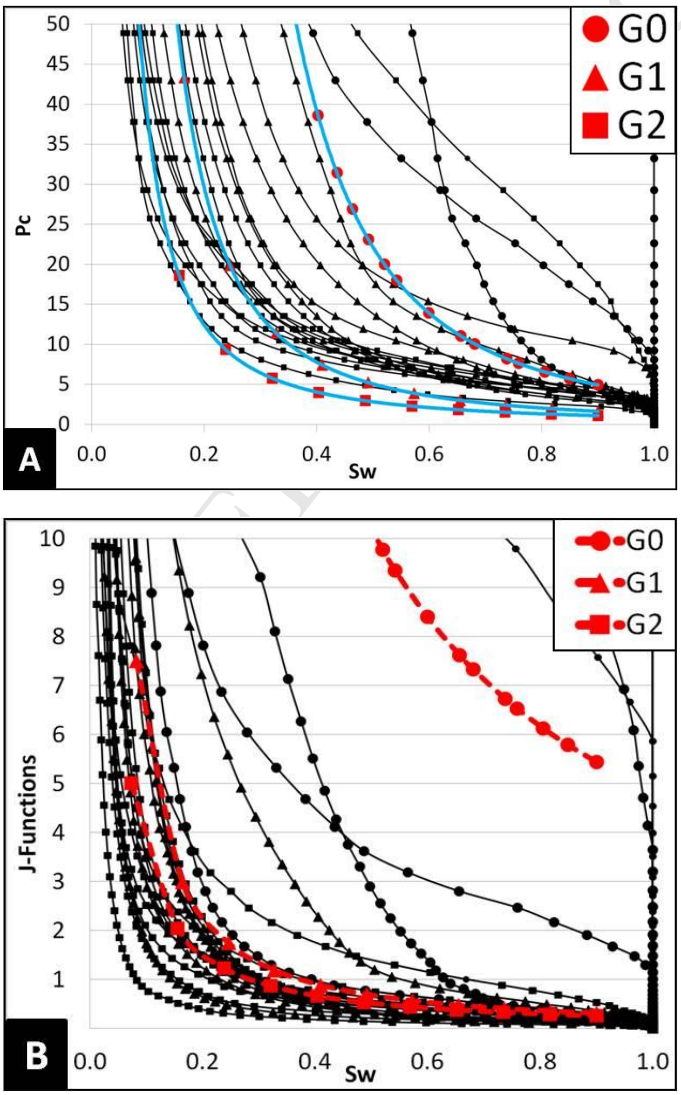

679
680 **Fig. 23.** (a) Average capillary pressure-saturation correlation curves obtained for the GeoPODS (b)
681 Average J functions obtained for the GeoPODS.

6.4. Implications towards fluid-in-place calculations and reservoir simulation

The capillary pressure-saturation relationships obtained for the GeoPODS using the two different methods discussed in the previous section were input as tables into the simulation model to test how this impacts the fluids-in-place volumes. The capillary pressure- and J-function-saturation correlations were applied to the saturation column from the relative permeability-saturation tables to calculate the P_c and J functions, respectively, for each of the GeoPODS. The input of J-function saturation tables was used by the simulator to compute the P_c values as

$$P_c = CF * J * T \cos\theta * \sqrt{\frac{\Phi}{k}}, \qquad (3)$$

where CF is the conversion factor and for capillary pressure in Psi (CF = 4.61678).

The impact of the different capillary pressure- and J-saturation correlations on the distribution of initial water saturation and therefore on the fluids-in-place calculation is demonstrated in Table 8. A difference of over 150 million STB of oil-in-place and up to 700 million MSCF of gas-in-place was observed. The impact of varying capillary pressure and J-function on the reservoir flow simulation results is shown in Figure 24. The J-function approach was tested using two GeoPODS permeability cases, one using the near-wellbore upscaled permeability transform shown in Figure 19a and one using a high permeability transform case. Recall that the impact of high- and low-endmember scenarios for the GeoPODS was tested. The simulation scenarios that incorporate GeoPODS and employ the respective J-functions showed better agreement of simulated and observed cumulative oil production compared to the simulation case that did not involve any rock-typing. The simulation scenario employing J-functions with high permeability transform case showed up to 22% increment in the cumulative oil production compared to the simulation case without rock-typing. These differences can be explained as follows: When the J-function correlations are used, the effect of block dependent porosity and permeability is accounted for during initialisation in the reservoir simulator (Eq. 3). This approach will produce a spatially varying transition zone which is not only a result of spatially varying capillary pressures but also the RQI. The RQI is in turn conditioned to the distribution of GeoPODS. Therefore, using the J-function approach that employs GeoPODS in the reservoir simulation provides internal consistency of the static reservoir properties, i.e., porosity and permeability, as well as the dynamic behaviour associated with capillary pressure and relative permeability. Hence saturation modelling and initialisation is more reliable in the reservoir simulation model. As a result, the simulation model predictions involving near-wellbore rock-typing and upscaling were in better agreement with the historic production data compared to the scenario without rock-typing. Figure 25 compares the difference between the simulated and historic cumulative fluid volumes in Field X after 22 years of production for the original geomodel and the updated model that employs GeoPODS.

716 **Table 8**. Sensitivity of volumes of oil- and gas-in-place to capillary pressure-saturation correlation.

Correlation method	STOIIP[*10^6 STB]	GIIP [*10^6 MSCF]
Capillary pressure-saturation	1138.9	2721.3
J-saturation using NWU permeability	965.7	2029
J-saturation using NWU permeability high case	1252.9	2685.2

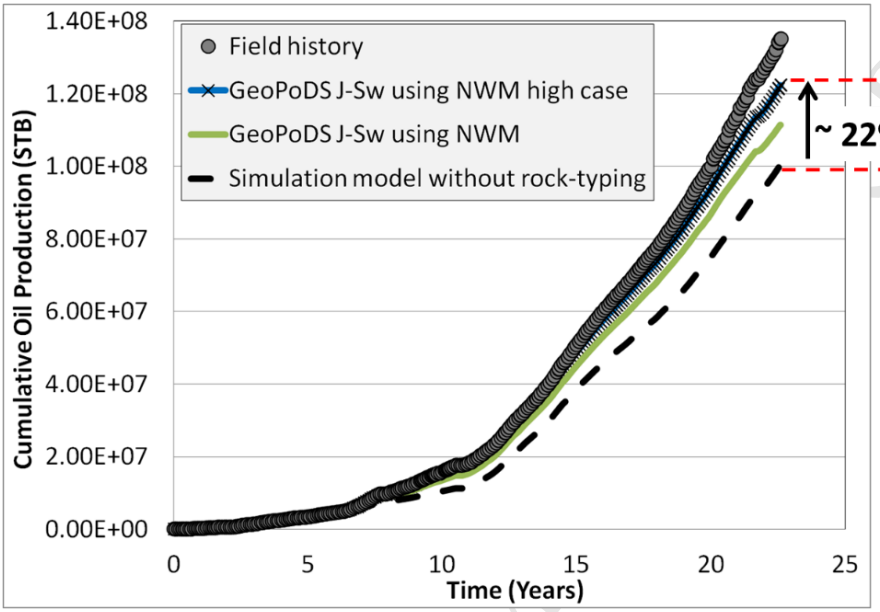

717
718 **Fig. 24.** Observed and simulated cumulative oil production curves in Field X. The GeoPODS
719 scenarios employing J-saturation method shows better agreement with historic data compared to the
720 simulation model that does not involve a near-wellbore rock-typing and upscaling workflow.

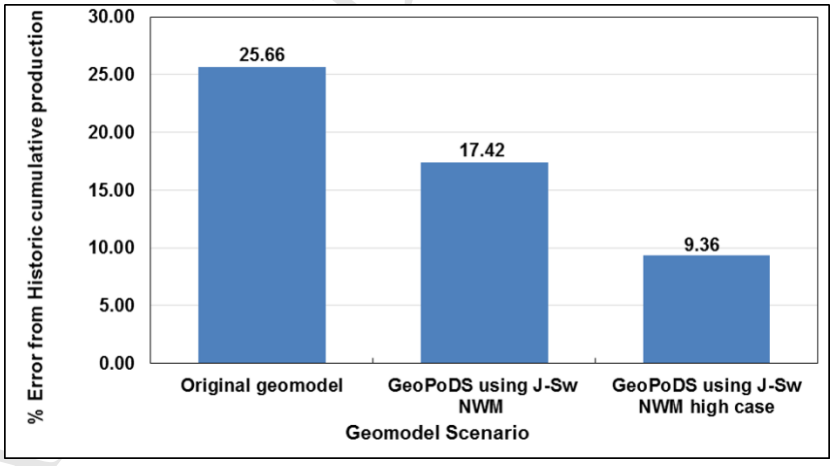

721

722 **Fig. 25.** The percentage error between the historic cumulative production value of Field X after 22
723 years of production and the geomodel scenarios with and without GeoPODS.

724 After 22 years of production, the simulated cumulative production value of the GeoPODS case using
725 J-functions and with NWM high permeability case showed only 9.46% error compared to the historic
726 data. In contrast, the error for the original geomodel was almost 25%. It must be emphasised that the
727 process of history matching yields a non-unique solution. In a way, similar results could have been
728 obtained by simply applying permeability multipliers in the simulation model and/or manipulating the

relative permeability end-points or the fault transmissibility values in the simulator. However, such manipulations, when done without any geological-petrophysical rationale, impose additional uncertainty to the model and render it less reliable for reservoir management and development studies, particularly if production mechanisms change. The near-wellbore rock-typing and upscaling workflow discussed in this study hence enables us to improve the characterisation and initialisation of the reservoir model prior to history-matching. This yielded a fit-for-purpose reservoir simulation model that incorporates small-scale geological structures in a consistent way and requires less modifications in order to obtain a good history match.

7. Conclusions

This study addressed key challenges associated with integrating reservoir rock-typing and simulation by employing a novel rock-typing workflow in conjunction with near-wellbore upscaling. Our near-wellbore rock-typing and upscaling workflow involves characterisation, modelling and upscaling of key small-scale geological-petrophysical heterogeneities into reservoir grid-block scale. This approach was demonstrated in a case study for a highly heterogeneous carbonate reservoir, Field X. We showed that our workflow improved the reservoir characterisation and simulation of the field.

Geological rock types (GeoRTs) were generated with the specific aim to account for the impact of late-burial corrosion. Late-burial corrosion is the key diagenetic phase in Field X and controls the evolution of reservoir properties. Petrophysical characterisation of GeoRTs allowed us to group them into near-wellbore rock types (NWRTs), which were then upscaled to the reservoir grid-block scale using the near-wellbore upscaling workflow. The upscaled porosity-permeability cluster was used to group the NWRTs with same porosity-permeability trends into Geological-Porosity Derived Systems (GeoPODS). GeoPODS are equivalent to upscaled plug-scale Hydraulic Flow Units and help to further define the Global Hydraulic Elements concept at the appropriate modelling scale for full field simulation models. The resulting GeoPODS scenarios hence incorporate the small-scale depositional and diagenetic heterogeneities in Field X. The GeoPODS were ultimately used to populate the reservoir geomodel and ensure that the static and dynamic reservoir properties are internally consistent within each GeoPODS. The porosity-permeability transforms, saturation-height functions and relative permeability curves individually tailored for each GeoPODS were employed in the reservoir simulation model for Field X. The updated reservoir simulation model was hence initialised consistently, providing an improved calculation of fluid in-place volumes. Simulation results indicate that reservoir simulation models that use GeoPODS in conjunction with J-functions yield cumulative production curves that agree well with the historic production data.

Overall, our study illustrates a new way of integrating multi-scale static and dynamic data pertinent to heterogeneous carbonate reservoirs seamlessly into a reservoir simulation model for improved

characterisation and dynamic calibration. The new simulation model is hence much better constrained to the reservoir geology and provides an improved geological-prior for subsequent history matching.

Acknowledgments

We acknowledge Foundation CMG for supporting the PhD project of Viswasanthi. We would like to extend our thanks to Alex Assaf and Zoe Watt from BG Group, Mohamed Ahmed, Zeyun Jiang and Eric Mackay from Heriot-Watt University for their valuable input into the project. Special thanks to the BG asset team for providing the necessary data and support required for the project. We also acknowledge CMG for IMEX, Schlumberger Information Solutions for access to Petrel and ECLIPSE, and to Geomodeling for access to SBED™.

References

Agar, S. M. & Geiger-Boschung, S. Jan 2015 *Fundamental Controls on Fluid Flow in Carbonates: Current Workflows to Emerging Technologies*. Agar, S. & Geiger, S. (eds.). London: Geological Society of London, p. 1-59 59 p. (Geological Society special publication; vol. 406)

Alsharhan, A.S. 1990. Geology and reservoir characteristics of Lower Cretaceous Kharaib Formation in Zakum Field, Abu Dhabi, United Arab Emirates. *In:* Brooks, J. (ed), *Classic Petroleum Provinces*. Geological Society Special Publications, **50**, 299–316.

Alsharhan, A.S. and Sadd, J. 2000. Stylolites in lower Cretaceous carbonate reservoirs. U.A.E. Society of Economic Paleontology and Mineralogy Special Publication, **69**, 185–207.

Amaefule, J. O., Altunbay, M., Tiab, D., Kersey, D. G., & Keelan, D. K. 1993. Enhanced Reservoir Description: Using Core and Log Data to Identify Hydraulic (Flow) Units and Predict Permeability in Uncored Intervals/Wells. Society of Petroleum Engineers. doi:10.2118/26436-MS.

Bear, J. 1972. Dynamics of Fluids in Porous Media. Elsevier, New York.

Calvert, S., & Ballay, G. 2011. Basic logs unlock complex carbonate pore properties. Society of Petrophysicists and Well-Log Analysts. *SPWLA-2011-MM*.

Chandra, V. 2014. Improving reservoir characterisation and simulation using near-wellbore upscaling. Ph.D. Thesis. Heriot-Watt University, Edinburgh.

Chandra, V., Corbett, P.W.M., Hamdi, H. and Geiger, S. 2013a. Improving reservoir characterisation and simulation with near-wellbore modelling. *SPE Reservoir Evaluation & Engineering*, **16 (2)**, 183-193, SPE Journal Paper 148104-PA.

Chandra, V., Steele, R., Milroy, P., Corbett, P.W.M. and Geiger, S. 2013b. Using near-wellbore modelling and dynamic calibration to improve permeability modelling in a giant carbonate field. Proceedings of 75th EAGE Conference & Exhibition incorporating SPE EUROPEC 2013, *TU 14 15*.

Chandra, V., Geiger, S., Corbett, P.W.M., Steele, R., Milroy, P., Barnett, A., Wright, P., Jain, P. 2013c. Using near-wellbore upscaling to improve reservoir characterisation and simulation in highly heterogeneous carbonate reservoirs. Proceedings of SPE Reservoir Characterisation and Simulation Conference, September 2013, *SPE 166033*.

Chandra, V., Wright, P. V., Barnett, A., Steele, R., Milroy, P., Corbett, P.W.M., Geiger, S., Mangione, A. 2015. Evaluating the impact of a late-burial corrosion model on reservoir permeability and performance in a mature carbonate field using near-wellbore upscaling. *Fundamental Controls on Fluid Flow in Carbonates: Current Workflows to Emerging Technologies*. Geological Society, London, Special Publications. doi 10.1144/SP406.11, 427-445.

Chilingarian, G.V., Torabzadeh, J., Rieke, H.H., Metghalchi, M., and Mazzullo, S.J. 1992. Interrelationships among surface area, permeability, porosity, pore size, and residual water saturation, *in* G.V. Chilingarian, S.J. Mazzullo, and H.H. Rieke, eds., Carbonate Reservoir Characterization: A Geologic-Engineering Analysis, Part I: Elsevier Publ. Co., Amsterdam, *Developments in Petroleum Science*, **30**, 379-397.

Corbett, P. W.M., Anggraeni, S. and Bowen, D. 1999. The use of the probe permeameter in carbonates - addressing the problems of permeability support and stationarity. *The Log Analyst*, **40**, 316-326.

Corbett, P. W.M. and Potter, D. K. 2004. Petrotyping: A basemap and atlas for navigating through permeability and porosity data for reservoir comparison and permeability prediction. Paper presented at International Symposium of the Society of Core Analysts, *SCA2004-30*.

Dabek, L. B. and Knepp, R. 2011. Bioturbation and Its Effects on Permeability in Wave-Dominated Shoreface Rocks of the Spring Canyon Member, Blackhawk Formation, Utah, USA. AAPG Search and Discovery Article # 50425. Proceedings of AAPG Annual Convention and Exhibition, Houston, Texas, USA, April 10-13, 2011.

Dunham, R.J. 1962. Classification of Carbonate Rocks According to Depositional Texture. In, W.E. Hamm (Ed.), Classification of Carbonate Rocks, A Symposium. *American Association of Petroleum Geologists*, 108-121.

Dykstra, H. & Parsons, R. L. 1950. The prediction of oil recovery by waterflooding. In Secondary Recovery of Oil in the United States, second edition, ed. 160-174. Washington, DC: API.

824 Elfenbein, C., Ringrose, P. S. & Christie, M. 2005. Small-scale reservoir modeling tool optimizes
825 recovery offshore Norway. *World Oil*, **226** (10), 45–50.

826 Fanchi, J. R. 2006. Fundamentals of Reservoir Simulation, In Principles of Applied Reservoir
827 Simulation (Third Edition), edited by John R. Fanchi, Gulf Professional Publishing, Burlington, Pages
828 162-186, ISBN 9780750679336, http://dx.doi.org/10.1016/B978-075067933-6/50012-X.

829 Gomes, J. S., Ribeiro, M. T., Strohmenger, C. J., Negahban, S., Kala, M. Z. 2008. Carbonate
830 Reservoir Rock Typing- The Link Betwen Geology and SCAL. *SPE Paper 118284*.

831 Honarpour, M.M., Chilingarian, G.V., and Mazzullo, S.J. 1992. Permeability and relative
832 permeability of carbonate reservoirs, *in* G.V. Chilingarian, S.J. Mazzullo, and H.H. Rieke, eds.,
833 Carbonate Reservoir characterization: A Geologic-Engineering Analysis, Part I: Elsevier Publ. Co.,
834 Amsterdam, *Developments in Petroleum Science*, **30**, 39x9-416.

835 Hollis, C., Vahrenkamp, V., Tull, S., Mookerjee A., Taberner, C., Huang, Y. 2010. Pore system
836 characterisation in heterogeneous carbonates: An alternative approach to widely-used rock-typing
837 methodologies. *Marine and Petroleum Geology*, **27**, 772-793.

838 Jodry, R.L. 1992. Pore geometry of carbonate rocks and capillary pressure curves (basic geologic
839 concepts), *in* G.V. Chilingarian, S.J. Mazzullo, and H.H. Rieke, eds., Carbonate Reservoir
840 Characterization: A Geologic-Engineering Analysis, Part I: Elsevier Publ. Co., Amsterdam,
841 *Developments in Petroleum Science*, **30**, 331-377.

842 Kazemi, A., Corbett, P.W.M., and Wood, R. 2012. New approach for geomodeling and dynamic
843 calibration of carbonate reservoirs using porosity determined system (PODS). Presented at 74th
844 EAGE conference and Exhibition, Copenhagen, Denmark, 4-7 June 2012.

845 Lucia, F. J. 1983. Petrophysical parameters estimated from visual description of carbonate rocks: a
846 field classification of carbonate pore space. *Journal of Petroleum Technology*, **35**, 626-637.

847 Mazullo, S. J. 2004. Overview of porosity evolution in carbonate reservoirs. *Kansas Geological*
848 *Society Bulletin*, **79**, 1-2.

849 Moshier, S.O. 1989. Development of microporosity in a micritic limestone reservoir, Lower
850 Cretaceous, Middle East. *Sedimentary Geology,* **63**, 217–240.

851 Nordahl, K., Ringrose, P.S. and Wen, R. 2005. Petrophysical characterisation of a heterolithic tidal
852 reservoir interval using a process-based modeling tool. *Petroleum Geoscience,* **11(1)**, 17-28.

Nordahl, K. 2004. A petrophysical evaluation of tidal heterolithic deposits: application of a near wellbore model for reconciliation of scale dependent well data. Ph.D. thesis. Norwegian University of Science and Technology, Trondheim.

Oates, M., Mishra, G., Sultana, N. and Nath, G. 2012. Resolving a permeability mismatch in a mature carbonate field. Proceedings of SPE Oil and Gas India Conference and Exhibition, Mumbai, March 2012, *SPE Paper 155458*.

Schmid, K.S., Geiger, S. 2013. Universal scaling of spontaneous imbibition for arbitrary petrophysical properties: Water-wet and mixed-wet states and Handy's conjecture. *Journal of Petroleum Science and Engineering*, **101**, 44-61, ISSN 0920-4105, http://dx.doi.org/10.1016/j.petrol.2012.11.015.

Skalinski, M., Kenter, J. A. M. 2015. Carbonate Petrophysical Rock Typing: Integrating Geological Attributes and Petrophysical Properties while Linking with Dynamic Behaviour. *Fundamental Controls on Fluid Flow in Carbonates: Current Workflows to Emerging Technologies*. Geological Society, London, Special Publications. **406,** 229-259.

Van der Land, C., Wood, R. A., Wu, K., van Dijke, MIJ., Jiang, Z, Corbett, P.W.M. and Couples, G.D. 2013. Modelling the permeability evolution of carbonate rocks. Marine and Petroleum Geology, Vol. 48, pp. 1-7, doi:10.1016/j.marpetgeo.2013.07.006.

Wardlaw, N.C. 1996. Factors affecting oil recovery from carbonate reservoirs and prediction of recovery, *in* G. V. Chilingarian, S.J. Mazzullo, and H.H. Rieke, eds., Carbonate Reservoir Characterization: A geologic-Engineering Analysis, Part II: Elsevier Publ. Co., Amsterdam, *Developments in Petroleum Science*, **44**, 867-903 .

Wen, R., Martinius, A.W., Naess, A. and Ringrose, P.S. 1998. Three-dimensional simulation of small-scale heterogeneity in tidal deposits – a process-based stochastic method. Proceedings of 4th Annual Conference of the International Association of Mathematical Geology, Ischia De Frede, Naples, 129-134.

Wright, V.P. and Barnett, A.J. 2011. Burial corrosion and porosity formation: from the seismic to micropore scale, but what processes do we blame*? Carbonate Geochemistry: Reactions and Processes in Aquifers and Reservoirs*. Karst Waters Institute Special Publication, **16**, 81-83.

Research Highlights:

- Novel rock-typing workflow integrated with near-wellbore upscaling.
- Workflow successfully applied to giant carbonate field with long production history
- Improved accuracy of FIP calculations during reservoir simulation.
- Improved geological-prior obtained for history matching and forecasting studies.